Title (120 characters):

Selective clearance of the inner nuclear membrane protein emerin by vesicular transport during ER stress

Authors: Abigail Buchwalter[1,2,3]*, Roberta Schulte[4], Hsiao Tsai[4], Juliana Capitanio[4], and Martin Hetzer[4]*

[1]Cardiovascular Research Institute, University of California San Francisco, San Francisco, CA, USA

[2]Department of Physiology, University of California San Francisco, San Francisco, CA, USA

[3]Chan Zuckerberg Biohub, San Francisco, CA, USA

[4]The Salk Institute for Biological Studies, La Jolla, CA, USA

*corresponding authors

Abstract

The inner nuclear membrane (INM) is a subdomain of the endoplasmic reticulum (ER) that is gated by the nuclear pore complex. It is unknown whether proteins of the INM and ER are degraded through shared or distinct pathways in mammalian cells. We applied dynamic proteomics to profile protein half-lives and report that INM and ER residents turn over at similar rates, indicating that the INM's unique topology is not a barrier to turnover. Using a microscopy approach, we observed that the proteasome can degrade INM proteins *in situ*. However, we also uncovered evidence for selective, vesicular transport-mediated turnover of a single INM protein, emerin, that is potentiated by ER stress. Emerin is rapidly cleared from the INM by a mechanism that requires emerin's LEM domain to mediate vesicular trafficking to lysosomes. This work demonstrates that the INM can be dynamically remodeled in response to environmental inputs.

Introduction

The biogenesis of roughly one-third of the cell's proteome takes place within the endoplasmic reticulum (ER) network. The ER is contiguous with the nuclear envelope (NE) membrane, a double bilayer membrane that defines the boundary of the nucleus. The NE is punctuated by nuclear pore complexes (NPCs) which control transport between the nuclear and cytoplasmic compartments. The outer nuclear membrane (ONM) and the bulk ER membrane network have a similar protein composition, including ribosomes that can be seen associated with the ONM. The inner nuclear membrane (INM), in contrast, is cloistered away from the bulk ER network by the NPC (Fig. 1A). Proteomic analyses suggest that hundreds of proteins are selectively concentrated at the INM(Schirmer, Florens, Guan, Yates, & Gerace, 2003), and mutations to these proteins cause a broad array of rare pathologies(Schreiber & Kennedy, 2013).

As the INM is devoid of ribosomes and translocation machinery, INM proteins must be synthesized in the ONM/ER and transported into the INM. Proteins concentrate at the INM by mechanisms including diffusion followed by stable binding to a nuclear structure,

49 such as chromatin or the nuclear lamina, or signal-mediated import through the
50 NPC(Katta, Smoyer, & Jaspersen, 2014). Transport across the NPC is a major kinetic
51 barrier to accumulation of proteins at the INM(Boni et al., 2015; Ungricht, Klann,
52 Horvath, & Kutay, 2015). While mechanisms of INM targeting have been extensively
53 studied, it is less clear how INM proteins are targeted for degradation if misfolded,
54 damaged, or mistargeted.
55
56 Protein folding is inefficient, and newly synthesized proteins often become terminally
57 misfolded and require degradation(Hegde & Zavodszky, 2019). Mature proteins also
58 become damaged or misfolded over time and require selective degradation and
59 replacement. Within the ER membrane network, the major degradation pathway is ER-
60 associated degradation, or ERAD. ERAD is initiated by poly-ubiquitination of a target
61 protein by an E3 ubiquitin ligase, followed by extraction from the membrane and
62 proteolysis by proteasomes in the cytosol(Hegde & Zavodszky, 2019). Flux through
63 ERAD helps to maintain organelle homeostasis and cell function by clearing damaged,
64 misfolded, or mislocalized proteins.
65
66 Recent work in *S. cerevisiae* has identified a small number of ubiquitin ligases that
67 target INM-localized proteins for degradation by ERAD, but the mammalian homologs
68 remain elusive, perhaps because of the massive expansion of the E3 ubiquitin ligase
69 family in recent evolution(Deshaies & Joazeiro, 2009). Degradation of mammalian INM
70 proteins also appears to rely on activity of the proteasome and on the ERAD ATPase
71 p97(Tsai, Zhao, Turner, & Schlieker, 2016), suggesting that mammalian INM proteins
72 may be subject to ERAD. However, we lack a broad understanding of the lifetimes of
73 INM proteins in this compartment and the pathways used for their degradation within
74 mammalian cells.
75
76 We sought to understand features of INM protein turnover in mammalian cells, and
77 applied both proteome-wide and targeted candidate approaches to address this
78 question. Here we show that the LEM domain protein emerin (EMD) is a rapidly
79 degraded constituent of the INM. We use EMD as a model for dissecting INM protein

80 turnover pathways and demonstrate that EMD is subject to both proteasome-dependent
81 and lysosome-dependent modes of degradation. We report that both misfolded and
82 normally folded variants of EMD are selectively exported from the INM and ER during
83 acute ER stress by vesicular transport through the secretory pathway and delivery to
84 the lysosome. These findings indicate that the INM sub-compartment senses and
85 responds to ER stress.
86
87 **Results**
88
89 **Trends in protein turnover across the NE / ER membrane network**
90 We first used a dynamic proteomic approach to understand trends in protein turnover
91 across ER sub-compartments. Since the nucleus is entirely disassembled during mitosis
92 in mammalian cells, we chose a system that would allow us to profile protein turnover in
93 the absence of cell division. We made use of the C2C12 myoblast culture system, which
94 can be induced to irreversibly differentiate into myotubes by serum
95 withdrawal(D'Angelo, Raices, Panowski, & Hetzer, 2009). We subjected these non-
96 dividing mouse muscle myotubes to a pulse-chase timecourse using stable isotope
97 labeling in cell culture (SILAC) (Ong & Mann, 2007) for timepoints ranging from 1 to 3
98 days (Fig. 1B, see Methods). Crude nuclear extracts were prepared and analyzed by
99 mass spectrometry, and the ratio of "old" ($^{13}C_6$-Lys, $^{15}N_4$ + $^{13}C_6$-Arg-labeled) to "new"
100 ($^{12}C_6$-Lys, $^{14}N_4$ + $^{12}C_6$-Arg-labeled) protein was quantified at the peptide level over time;
101 peptides that passed stringent quality control filters were retained for estimation of half-
102 lives by a linear regression fitting method(Dörrbaum, Kochen, Langer, & Schuman,
103 2018)(see Methods). We evaluated 1677 proteins and predicted half-lives over a wide
104 range, from less than a day to greater than 15 days (Fig. 1E, Table S3). Linear
105 regression performs well when a line can be fit with high fidelity and a non-zero slope is
106 detectable; these conditions were generally met for proteins with predicted half-lives
107 ranging from 1 to 8 days. We observed more frequent deviations in linearity at the low
108 extreme (predicted $t^{1/2}$ <1 day) and slopes approaching zero at the high extreme
109 (predicted $t^{1/2}$ > 8 days) (Figure 1 – figure supplement 1). We expect that these factors
110 limit the precision of half-life determination below 1 day and above 8 days from our 3-

111 day timecourse. The median turnover rate that we observed (2.4 days) corresponds well
112 with previous analyses in non-dividing mammalian cell cultures(Cambridge et al., 2011).
113
114 We observed some extremes in protein stability that are consistent with previous
115 reports; for example, the long-lived nuclear pore complex component Nup160(Toyama
116 et al., 2013) was in the top 10% of predicted half-lives, with a calculated half-life of
117 approximately 18 days (Fig. 1C, F, Table S1). Near the other extreme, we observed that
118 the enzyme topoisomerase 2α (Topo2α) had a predicted half-life in the bottom 10%, of
119 less than 1 day (Fig. 1D, F). This is consistent with this enzyme's known regulation by
120 ubiquitination and proteolysis(Gao et al., 2014).
121
122 Having established this framework, we then quantified the turnover kinetics of known
123 inner nuclear membrane (INM) proteins. For this analysis, we focused on proteins
124 whose preferential enrichment in this membrane compartment had been experimentally
125 verified; we identified ten such proteins in our dataset (see Table S1) and determined
126 their half-lives (see Methods). We observed half-lives for these proteins ranging from
127 8.8 days (nurim) to 1.5 days (emerin) (Fig. 1G). While very little is known about nurim's
128 function, its intrinsic biophysical properties may contribute to its long half-life: nurim
129 contains six transmembrane domains, is extremely insoluble(Hofemeister & O'Hare,
130 2005), and diffuses very slowly within the INM(Rolls et al., 1999). Emerin (EMD) is a
131 founding member of the LEM domain family of INM proteins with essential functions in
132 muscle development(Brachner & Foisner, 2011). Unlike nurim, EMD is a small (~25
133 kDa), single-pass, tail-anchored transmembrane protein that diffuses freely through the
134 NPC and enriches at the INM by virtue of its affinity for lamin A(Vaughan et al., 2001).
135
136 Given the INM's status as a restricted sub-compartment of the ER, we reasoned that it
137 might be possible that INM proteins would be generally less accessible to protein
138 turnover than ER membrane proteins. Alternatively, similarly effective turnover in both

Figure 1. Proteomic analysis of nuclear envelope protein half-lives in C2C12 myotubes.

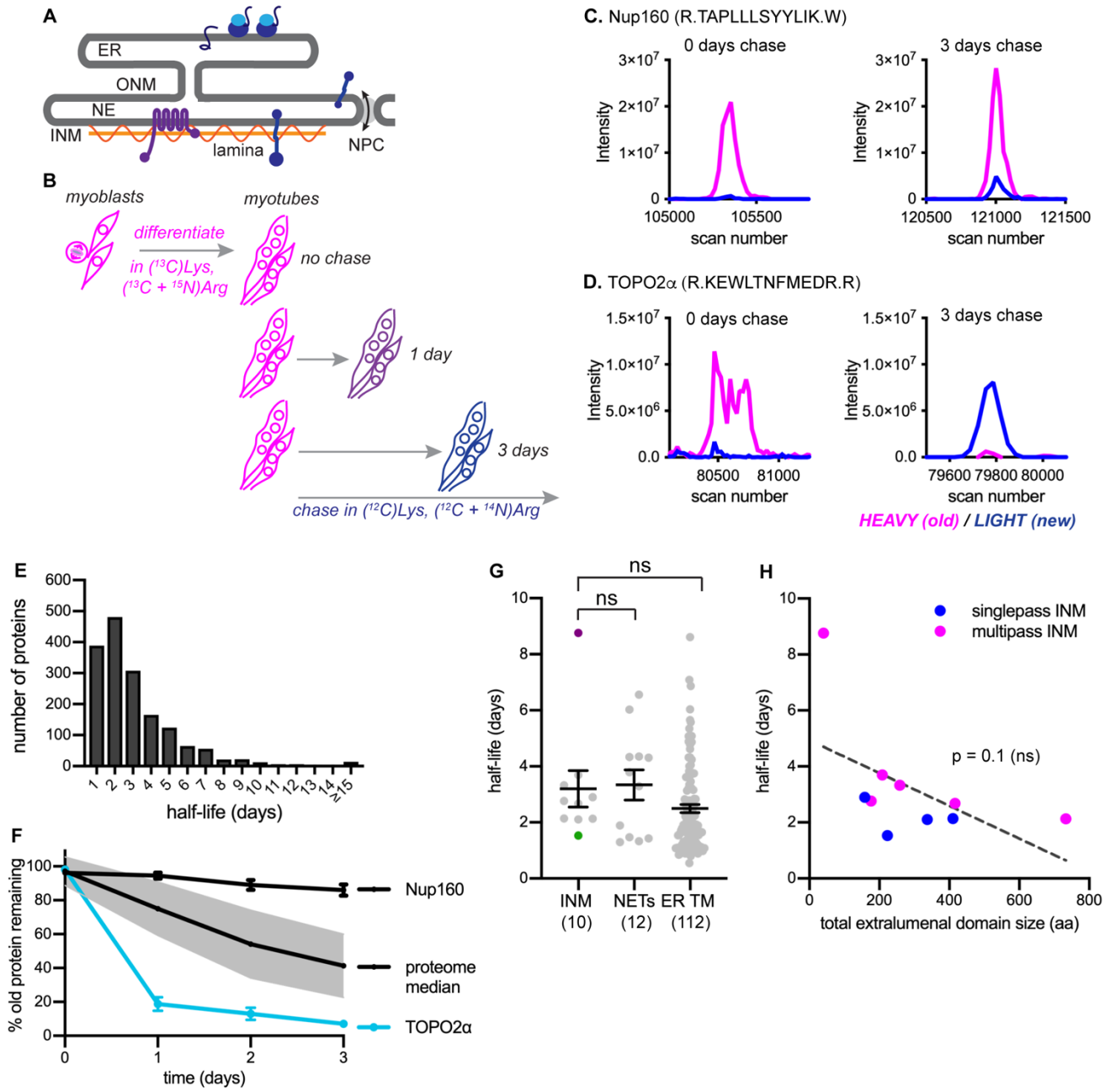

139

Figure 1. Dynamic proteomic analysis of inner nuclear membrane protein turnover. (A) Diagram of the ER with associated ribosomes, the NE composed of the ONM and INM, the NPCs, and the underlying nuclear lamina. INM proteins are synthesized in the ER, pass through the NPC, and enrich at the INM. (B) Overview of dynamic SILAC labeling experimental design. C2C12 mouse myoblasts were cultured for 5 population doublings in medium containing $^{13}C_6$-lysine and $^{13}C_6$, $^{15}N_4$-arginine to completely label the proteome. After 3 days of culturing under differentiating conditions to generate non-dividing myotubes, cultures were switched to chase medium containing ^{12}C-lysine and ^{12}C, ^{14}N-arginine for 1 to 3 days. Nuclear extracts were prepared at day 0, day 1, day 2, and day 3 for proteomic identification. (C,D) Representative peptide scans for a slowly degraded protein (Nup160) and (D) for a rapidly degraded protein (Topo2α) at the starting and ending points of the experiment outlined in (B). (E) Histogram of calculated half-lives for 1677 proteins with a median half-life of 2.4 days. (F) Features of nuclear proteome turnover. Median turnover behavior of 1677 proteins detected in at least three timepoints with at least one peptide (black line) with 1 standard deviation (gray); compared to turnover of the slowly exchanged protein Nup160 (black) and the rapidly exchanged protein Topo2α (blue). Error bars indicate SEM. (G) Calculated half-lives of 10 *bona fide* INM proteins, ranging from slowly degraded (nurim, purple) to rapidly degraded (emerin, green); 12 nuclear envelope transmembrane proteins (NETs) identified as NE residents by subtractive proteomics (see Schirmer, 2003); and 112 ER membrane proteins. ns indicates lack of statistical significance by Mann-Whitney test. Error bars indicate SEM. (H) There is no significant correlation between extraluminal domain size of INM proteins and their half-lives. See also Source Data 1-2, Supplementary Files 1-3, and Figure 1 – figure supplement 1.

compartments might support the possibility that turnover can occur *in situ* at the INM. ER membrane proteins were well represented in our dataset, as a significant proportion of ER membranes remain attached to and co-purify with nuclei(Schirmer et al., 2003). We could thus query whether INM proteins exhibited distinct turnover kinetics from membrane proteins of the bulk ER by comparing INM and ER transmembrane protein half-lives. We also compared *bona fide* INM proteins to proteins that had been identified as preferentially associated with either the inner or outer bilayer of the nuclear envelope (NE) membrane by comparative proteomics(Schirmer et al., 2003), termed NE transmembrane proteins (NETs). Altogether, these analyses indicate that INM proteins do not exhibit unique turnover kinetics as a protein class, compared to ER membrane proteins in general or to the overlapping designation of NETs (Fig. 1G).

The size of INM proteins determines whether a protein must rely on signal-mediated transport through the NPC(Katta et al., 2014), and live imaging assays indicate that INM proteins with larger nucleoplasm-facing domains move more slowly across the NPC barrier(Boni et al., 2015; Ungricht et al., 2015). If transit across the NPC and out of the

157 INM were a prerequisite for turnover in the bulk ER, we reasoned that turnover
158 efficiency would also exhibit some dependence on protein size, because of the
159 relationship between protein size and transport efficiency between the two
160 compartments. The short half-life and small size of EMD is in line with this possibility.
161 Our dataset of INM proteins included four single-pass INM and six multi-pass INM
162 proteins, with total size of extraluminal domains ranging from 40 amino acids to 733
163 amino acids (Table S5). If export out of the NPC were a prerequisite for INM protein
164 turnover, we reasoned that half-life should increase as the bulk of nucleoplasm-facing
165 domains increases. We found no evidence for such a correlation (Fig. 1H). We infer
166 from this analysis that other factors distinct from monomeric protein size regulate
167 protein turnover rate. This indicates that for INM proteins, export out of the INM is not a
168 rate-limiting step for protein turnover. Rather, this is consistent with evidence in *S.*
169 *cerevisiae*(Foresti, Ruggiano, Hannibal-Bach, Ejsing, & Carvalho, 2013; Khmelinskii,
170 Blaszczak, Pantazopoulou, Fischer, Omnus, Le Dez, Brossard, Gunnarsson, Barry,
171 Meurer, Kirrmaier, Boone, Huber, Rabut, Ljungdahl, & Knop, 2014a) and in mammalian
172 cells(Tsai et al., 2016)that turnover of INM proteins can take place *in situ* at the INM.
173

174 **Recombination-induced tag exchange confirms INM protein lifetimes**

175 We observed a wide range of half-lives for INM proteins in our proteomic analyses (Fig.
176 1G), with the polytopic INM protein nurim turning over most slowly and the single-pass
177 INM protein EMD turning over most rapidly. To directly visualize these relative
178 differences in protein stability, we used recombination-induced tag exchange (RITE)
179 (Toyama et al., 2019; Verzijlbergen et al., 2010) (Fig. 2A) to perform a microscopy-
180 based pulse-chase experiment. We expressed either nurim or EMD in a cassette
181 encoding two C-terminal epitope tags separated by LoxP sites and by a stop codon,
182 such that the resulting transcript will encode a protein that will be C-terminally tagged
183 with the first tag. Upon adenoviral introduction of Cre recombinase, the RITE cassette is
184 recombined to remove the first tag and position the second tag downstream of the open
185 reading frame, so that all newly synthesized mRNA encodes a protein marked with the
186 second tag.

Figure 2. RITE analysis of INM proteins enables visualization of proteasome-dependent turnover.

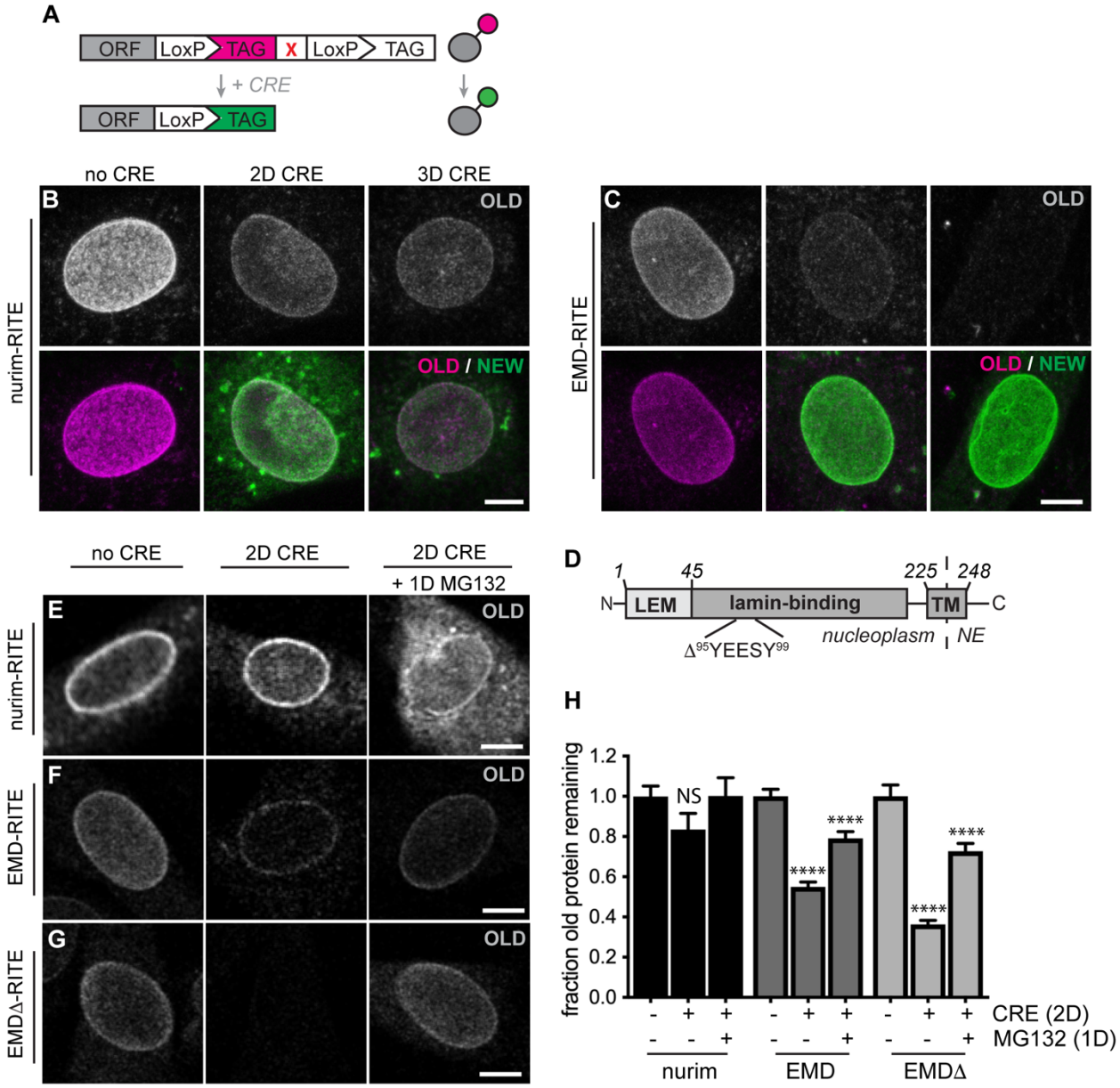

187

Figure 2. RITE analysis of INM proteins corroborates protein turnover determined by proteomics. (A) Schematic of recombination-induced tag exchange (RITE) expression cassette for visualizing protein turnover using Cre recombinase-mediated tag switching. (B-C) RITE timecourses of nurim-RITE (B) and EMD-RITE (C) in quiescent C2C12 cells. Maximum intensity projections of confocal z-series shown. (D) Diagram of emerin domain organization and position of EDMD-linked deletion mutant (EMD∆95-99) within the lamin-binding domain. (E-G) RITE timecourses of nurim-RITE (E), EMD-RITE (F), and EMD∆-RITE (G) with or without 1 day of cotreatment with the proteasome inhibitor MG132 (right panels). Single confocal z-slices shown. (H) Quantification of normalized intensity of old NE-localized RITE-tagged protein in maximum intensity projections of confocal z series acquired across the conditions shown in (E-G). Bars indicate average values with error bars indicating SEM for N > 42 cells per condition from 2 independent experiments. **** indicates p-value < 0.0001 (by t-test) for comparison between untreated and treated conditions. Scale bar, 10 μm. See also Figure 2 – figure supplement 1.

This enables simultaneous tracking of older and newer pools of protein that were synthesized before and after Cre addition, respectively (Toyama et al., 2019; Verzijlbergen et al., 2010). Using this approach, we visualized the rate of decline in the fluorescence intensity of “old” myc-tagged nurim or EMD over several days in quiescent C2C12 cells. Consistent with our proteomic observations, we observed that RITE-tagged nurim decayed significantly more slowly than RITE-tagged EMD at the NE (Fig. 2B-C, H).

The RITE system allows unambiguous dissection of the fates of maturely folded protein as well as nascent, newly synthesized protein. Recent work in yeast(Foresti et al., 2013; Khmelinskii, Blaszczak, Pantazopoulou, Fischer, Omnus, Le Dez, Brossard, Gunnarsson, Barry, Meurer, Kirrmaier, Boone, Huber, Rabut, Ljungdahl, & Knop, 2014a) and in mammalian cells(Tsai et al., 2016) strongly suggests that INM proteins are subject to proteasome-mediated degradation via the ERAD pathway. The RITE system provides a means to distinguish the effects of proteasome inhibition on maturely folded proteins by inhibiting the proteasome after RITE tag switching, and monitoring the effects on maturely folded proteins. Mature nurim-RITE decreases only modestly within 2 days of tag switching, but co-incubation with the proteasome inhibitor MG132 for 1 day causes accumulation of nurim-RITE through the NE and ER (Fig. 2E, H). Maturely folded EMD-RITE diminishes significantly at the NE within 2 days of tag switching but is partially stabilized at the NE in the presence of MG132 (Fig. 2F, H). This indicates that mature, INM-localized proteins can be degraded in a proteasome-

211 dependent pathway *in situ* at the INM. Notably, abundant proteasomes have been
212 observed along the INM in cryo-EM studies and could possibly engage with substrate
213 there(Albert et al., 2017). This is also consistent with a recent report that an unstable
214 INM protein mutant accumulates within the nucleus of mammalian cells when the
215 proteasome is inhibited(Tsai et al., 2016).
216
217 **Identification of a model substrate for dissecting INM protein turnover**
218 In order to gain more insight into the pathways that control INM protein turnover in
219 mammalian cells, we chose to focus on EMD for its relatively fast turnover rate (Fig. 1G,
220 Table S1) and for the variety of disease-linked mutations to EMD that appear to
221 influence protein stability(Fairley, Kendrick-Jones, & Ellis, 1999). Loss-of-function
222 mutations to EMD cause Emery-Dreifuss muscular dystrophy (EDMD) (Bonne &
223 Quijano-Roy, 2013). In some cases, EDMD-linked mutations cause loss of detectable
224 EMD protein without affecting mRNA levels, suggesting that these mutations might
225 cause misfolding and degradation of EMD(Fairley et al., 1999). We sought to identify
226 such an EDMD-linked EMD variant for use as a model substrate for dissecting INM
227 protein turnover. We selected a small in-frame deletion (Δ95-99) within EMD's lamin-
228 binding domain (Fig. 2D) that had been previously shown to localize to the NE when
229 ectopically expressed(Fairley et al., 1999). Consistently, when we expressed either
230 EMD-GFP or EMDΔ95-99-GFP in C2C12 cells, we observed similar enrichment at the
231 NE (Figure 2 – figure supplement 1). Further, both protein variants exhibited identical
232 residence times at the NE as assayed by fluorescence recovery after photobleaching
233 (FRAP) analysis (Figure 2 – figure supplement 1). Directly monitoring the stability of
234 EMDΔ95-99 by RITE tagging indicates that it disappears from the NE faster than wild
235 type EMD (Fig. 2G), but is also stabilized at the NE by proteasome inhibition (Fig. 2G-
236 H). These observations indicate that EMDΔ95-99 is an unstable EMD variant that
237 resides within the INM. We next moved to dissect that pathway(s) involved in EMDΔ95-
238 99 degradation.
239
240 **Proteasome-dependent and proteasome-independent modes of emerin clearance**

241 Misfolded ER resident proteins are cleared by the ER-associated degradation (ERAD)
242 pathway. ERAD clients are marked for degradation by ubiquitination, extracted from the
243 ER membrane by the ATPase enzyme p97, and degraded by the proteasome in the
244 cytosol(Ruggiano, Foresti, & Carvalho, 2014). INM proteins may also be targeted to an
245 arm of the ERAD pathway in mammalian cells (Tsai et al., 2016), and our data indicates
246 that multiple INM proteins are stabilized *in situ* by proteasome inhibition. However,
247 ubiquitin ligase(s) that recognize INM-localized substrates in mammalian cells have not
248 been identified.
249
250 To sensitively probe factors that influence INM protein stability, we tracked the stability
251 of GFP-tagged EMD variants. When *de novo* protein synthesis was blocked by
252 cycloheximide (CHX), we observed rapid loss of EMDΔ95-99-GFP within 4-8 hours (Fig.
253 3A-B) while wild type EMD remained stable (Figure 3 – figure supplement 1). This loss
254 is blunted by co-treatment with the proteasome inhibitor MG132 (Fig. 3A, third panel),
255 consistent with our observations that INM protein turnover is slowed by proteasome
256 inhibition using the RITE system (Fig. 2E-G). If EMDΔ95-99-GFP is directed to the
257 proteasome through ERAD, inhibition of earlier steps in this pathway should similarly
258 cause accumulation of EMDΔ95-99-GFP. Indeed, pharmacological inhibition of p97 with
259 the drug eeyarestatin I(Wang, Li, & Ye, 2008) causes modest accumulation of EMDΔ95-
260 99 and of higher molecular weight species, a similar effect to proteasome inhibition itself
261 (Fig. 3B). In contrast, the drug kifunensine, which prevents ERAD targeting of misfolded
262 glycosylated proteins(Fagioli & Sitia, 2001), has no effect on EMDΔ95-99-GFP levels as
263 would be expected given the lack of glycosylation sites within EMD's small luminal
264 domain (Fig. 3B).
265
266 E3 ubiquitin ligases transfer ubiquitin to ERAD substrates, and each E3 ligase exhibits
267 preference for a small number of substrates. A few E3 ligases have been implicated in
268 ERAD of INM-localized substrates in yeast, including Doa10 and Asi1(Khmelinskii,
269 Blaszczak, Pantazopoulou, Fischer, Omnus, Le Dez, Brossard, Gunnarsson, Barry,
270 Meurer, Kirrmaier, Boone, Huber, Rabut, Ljungdahl, & Knop, 2014b). MARCH6 is a

271 mammalian ortholog of Doa10(Zattas, Berk, Kreft, & Hochstrasser, 2016). Mammalian

Figure 3. Acute ER stressors destabilize mutant emerin protein levels.

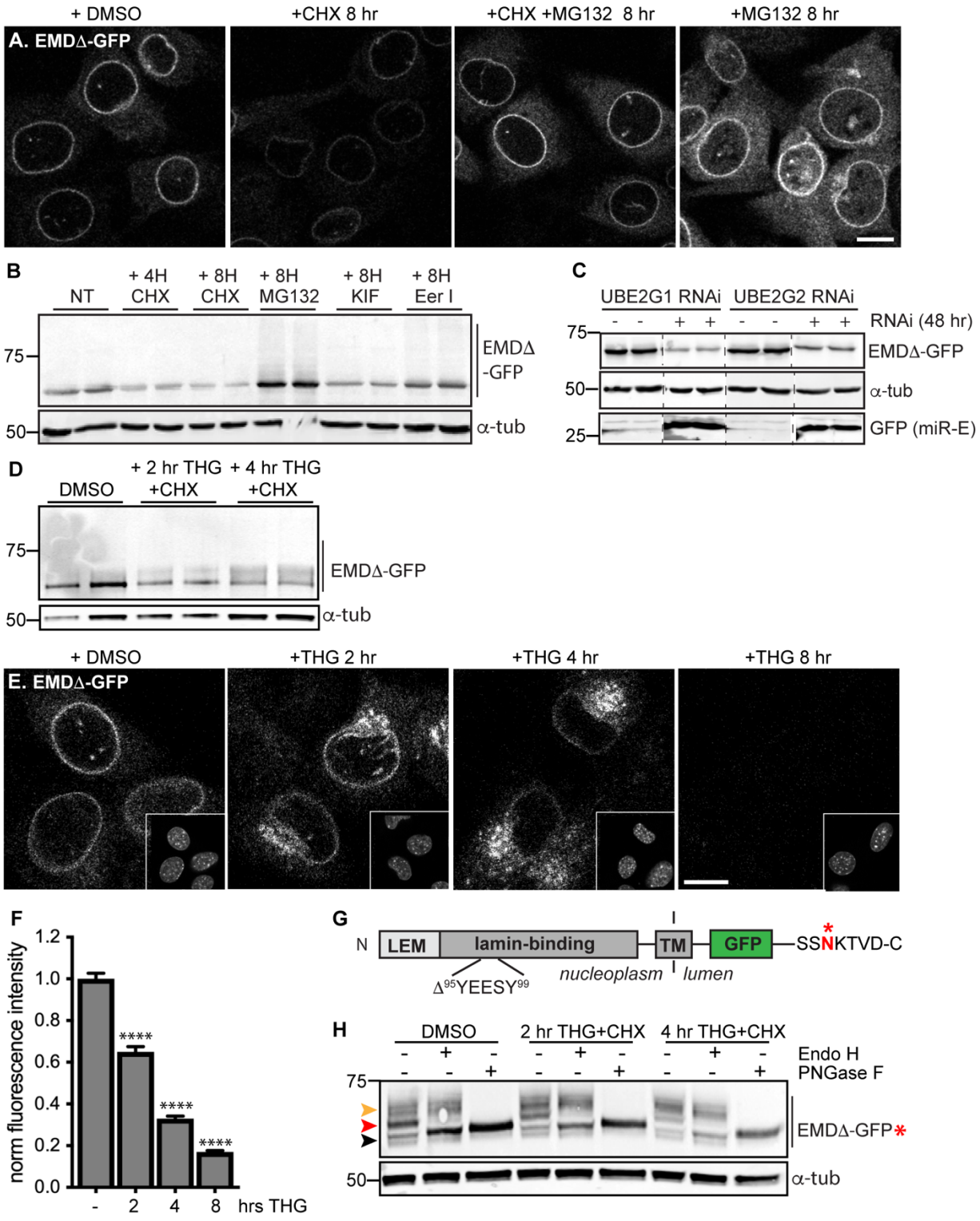

272

273

Figure 3. Acute stressors destabilize mutant emerin protein levels. (A) C2C12 cells stably expressing EMDΔ-GFP and treated with DMSO vehicle control, CHX alone, CHX and MG132, or MG132 alone for 8 hours. All images were acquired using the same laser power and detector gain settings. Single confocal z slices shown. (B) Western blot analysis of protein levels in C2C12 cells stably expressing EMDΔ-GFP and treated with DMSO vehicle, the translation inhibitor CHX, the proteasome inhibitor MG132, the p97 ATPase inhibitor eeyarestatin, or the glycosylation trimming inhibitor kifunensine for the time periods shown. α-tubulin shown as loading control. (C) Western blot analysis of U2OS cells stably expressing EMDΔ-GFP and doxycycline-inducible RNAi targeting the E2 ubiquitin ligases UBE2G1 and UBE2G2 and treated with DMSO vehicle control (-) or with doxycycline (+) for 48 hours. Free GFP indicates RNAi induction. α-tubulin shown as loading control. (D) Western blot detection of EMDΔ-GFP levels in cells treated with DMSO vehicle, or co-treated with CHX and the ER stress inducer THG for the time periods shown. α-tubulin shown as loading control. (E) C2C12 cells stably expressing EMDΔ-GFP and treated with vehicle control or with THG for the time periods shown. Insets show nuclei in the same ~50 μm field of view stained with Hoechst. All images acquired using the same laser power and detector gain settings; single confocal z slices shown. (F) Quantification of total NE-localized GFP fluorescence in maximum intensity projections of confocal z slices acquired across the conditions shown in (E) for N > 410 cells per condition. (G) Diagram of emerin domain organization and the sequence of an inserted C-terminal glycosylation sequence derived from the opsin protein, with glycosylation acceptor site marked (*). (H) Analysis of EMDΔ-GFP* glycosylation state in cells subjected to treatment with DMSO vehicle control or CHX and THG cotreatments for the times indicated. Red arrowhead indicates EndoH-sensitive glycosylated state of EMDΔ-GFP*; orange arrowhead indicates EndoH-resistant states of EMDΔ-GFP*; black arrowhead indicates deglycosylated EMDΔ-GFP*. α-tubulin shown as loading control. Numbers to left of blots indicate molecular weights in kDa. Scale bars in micrographs indicate 10 μm. See also Figure 3 – figure supplement 1, 2, and 3.

orthologs of Asi1 have not been identified. Based on iterative sequence homology analysis through the MetaPhORs database(Pryszcz, Huerta-Cepas, & Gabaldón, 2010) we identified two possible Asi1 homologs: Rnf26 and CGRRF1. We depleted MARCH6, Rnf26, and CGRRF1 with short interfering RNA (siRNA), but observed no effect on EMDΔ95-99 protein levels (Figure 3 – figure supplement 2), suggesting that these ligases do not catalyze EMD turnover, or alternatively that multiple E3 ligases are redundant in this process. Importantly, the broad group of ERAD-implicated E3 ligases rely on a handful of E2 ubiquitin conjugating enzymes for ubiquitin transfer. These E2 ligases – four in mammals – thus represent a key control point for ERAD(Christianson, Olzmann, Shaler, Sowa, Bennett, Richter, Tyler, Greenblatt, Wade Harper, et al., 2011b; Leto et al., 2019). We targeted these four E2 ubiquitin ligases by siRNA transfection (Figure 3 – figure supplement 2) and a subset of these by inducible RNAi using a potent microRNA-based system (Fellmann et al., 2013) and analyzed the effects on EMDΔ95-99-GFP levels. To our surprise, knockdown of UBE2G1, UBE2G2,

288 UBE2J1, and UBE2J2 either did not stabilize or instead decreased EMDΔ95-99-GFP
289 levels (Fig. 3C; Figure 3 – figure supplement 2). This finding suggests that when ERAD
290 is perturbed, EMD variants can be cleared by an alternative pathway.
291
292 **Emerin is subject to rapid stress-dependent clearance from the ER and NE**
293 Global inhibition of ERAD places profound protein folding stress on the ER membrane
294 network and induces the unfolded protein response (UPR) (Christianson, Olzmann,
295 Shaler, Sowa, Bennett, Richter, Tyler, Greenblatt, Harper, et al., 2011a). We considered
296 whether direct induction of ER stress was sufficient to accelerate the turnover of
297 EMDΔ95-99-GFP. We tested the effect of the ER stressor thapsigargin (THG), which
298 disrupts ER homeostasis by causing release of Ca2+ from the ER lumen, on EMDΔ95-
299 99 protein stability. Compared to CHX treatment alone (Figure 3 – figure supplement 1),
300 THG co-treatment further destabilized EMDΔ95-99-GFP (Fig. 3D). Strikingly, when we
301 tracked EMDΔ95-99 protein localization by time-lapse microscopy (Fig. 3E), it became
302 apparent that NE localization of EMDΔ95-99 significantly decreases within 2 hours of
303 THG treatment, concomitant with accumulation in a perinuclear membrane
304 compartment that morphologically resembles the Golgi apparatus. By 8 hours after THG
305 administration, EMDΔ95-99 was undetectable (Fig. 3E-F). These data suggest that
306 under conditions of ER stress, EMDΔ95-99 is cleared from the NE/ER membrane
307 network by transport out of the ER and eventual disposal of the protein in a post-ER
308 compartment.
309
310 **Acute ER stress reroutes emerin through the secretory pathway**
311 We took several approaches to test the possibility that EMDΔ95-99 leaves the NE/ER
312 network during ER stress. Firstly, we made use of the characteristic sugar modifications
313 that occur as cargoes progress through the secretory pathway to determine whether
314 EMDΔ95-99 accesses post-ER compartments. Since the short lumenal domain of EMD
315 lacks a glycosylation consensus site, we engineered the glycosylation site from the
316 opsin protein(Bulbarelli, Sprocati, Barberi, Pedrazzini, & Borgese, 2002) (SSNKTVD)
317 onto the lumen-facing C terminus of EMDΔ95-99. If EMDΔ95-99 is retained in the ER,
318 all of its N-linked glycans should remain sensitive to the trimming enzyme Endo H. On

319 the other hand, if EMDΔ95-99 exits the ER, its N-linked glycans will be elaborated with
320 further modifications so that Endo H can no longer trim them. These glycosylation states
321 can be detected as progressive increases in molecular weight, and can be completely
322 removed by incubation with the enzyme PNGase F. This engineered variant, EMDΔ95-
323 99-GFP*, localizes normally to the NE and also disappears from the NE upon ER stress
324 induction (Figure 3 – figure supplement 3). In unstressed cells, EMDΔ95-99-GFP* is
325 predominantly observed in an Endo H-sensitive glycosylation state (Fig. 3H, red
326 arrowhead), with a minor pool of Endo H-resistant protein (Fig. 3H, orange arrowhead).
327 In contrast, EMDΔ95-99-GFP* shifts progressively to a higher molecular weight, Endo
328 H-resistant state over 2 to 4 hours of co-treatment with CHX and THG. This indicates
329 that ER stress induction increases the proportion of EMDΔ95-99 that exits the NE/ER
330 and samples post-ER compartments.
331
332 Upon ER stress induction, EMDΔ95-99-GFP accumulates in a perinuclear domain that
333 resembles the Golgi apparatus (Fig. 3E). We evaluated the extent of colocalization of
334 EMDΔ95-99-GFP with the medial Golgi resident protein giantin in untreated cells and
335 cells that had been treated with THG for 2-4 hours (Fig. 4A-C). In untreated cells,
336 EMDΔ95-99-GFP was not detectable in the Golgi, but THG treatment rapidly induced
337 Golgi colocalization as NE-localized EMDΔ95-99 levels decreased (Fig. 4A-C).
338 Comparing GFP fluorescence intensity in the Golgi *versus* the NE over time revealed
339 that ER stress induces significant enrichment of EMDΔ95-99-GFP in the Golgi
340 accompanied by loss from the NE within 2 hours (Fig. 4D).
341
342 EMDΔ95-99 could be delivered to the Golgi by vesicular transport from the ER.
343 Transport between the ER and the Golgi is mediated by packaging of cargoes into
344 COP-coated vesicles (Barlowe & Miller, 2013), a process which can be inhibited by the
345 drug brefeldin A (BFA). BFA acts by disrupting COPI vesicle formation, leading to the
346 collapse of the Golgi into the ER membrane network (Chardin & McCormick, 1999). To
347 test whether clearance of EMDΔ95-99-GFP from the NE/ER requires vesicle-mediated
348 ER-to-Golgi transport, we co-incubated cells expressing EMDΔ95-99-GFP with THG
349 and BFA. Strikingly, co-treatment with BFA nearly quantitatively reversed loss of

EMDΔ95-99-GFP from the NE (Fig 4E-F). Taken together with the time-dependent enrichment of EMD variants in the Golgi apparatus (Fig. 4A-C), and the time-dependent accumulation of more complex N-glycosylated variants of EMDΔ95-99-GFP* (Fig. 3H), this indicates that under ER stress, EMD variants can be cleared from both the NE and ER by vesicular transport through the Golgi.

Figure 4. Stress-induced clearance of mutant emerin from the NE and ER involves the secretory pathway

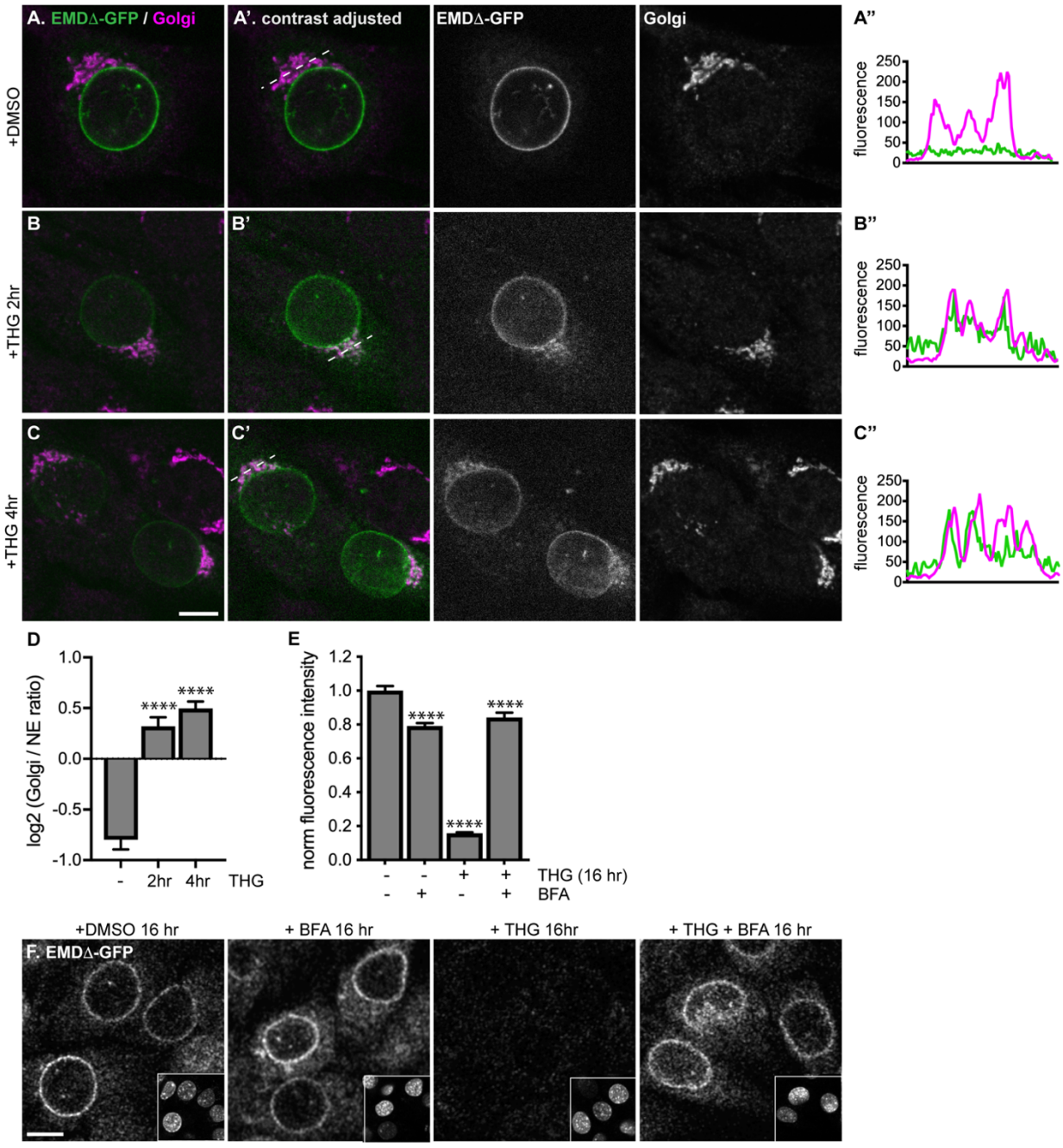

Figure 4. Stress-induced clearance of mutant emerin from the ER and NE involves the secretory pathway. (A-C) Representative confocal slices of cells stably expressing EMDΔ-GFP, treated with DMSO or THG for the indicated times and costained for giantin to mark the Golgi (magenta). All images were acquired using the same laser power and detector gain settings. (A'-C') Are contrast-adjusted to show relative levels of EMDΔ-GFP in NE and Golgi. Dotted lines mark positions of linescans in (A''-C''). (D) Quantification of GFP fluorescence intensity abundance ratio in Golgi *versus* NE in single, non-contrast-adjusted z slices over THG treatment timecourse. Columns indicate average with error bars indicating SEM for N > 37 cells from 2 independent experiments. **** indicates p-value < 0.0001 compared to untreated (by t-test). (E-F) Representative confocal slices of cells stably expressing EMDΔ-GFP (F) after 16 hours of treatment with DMSO vehicle control, THG, BFA, or co-treatment with THG and BFA. All images were acquired using the same laser power and detector gain settings. Insets show nuclei in the same ~50 μm field of view stained with Hoechst. (E) Quantification of GFP fluorescence intensity at the NE in maximum intensity projections of confocal z series acquired across the conditions represented in (F). Columns indicate average with error bars indicating SEM for N > 386 cells from 3 independent experiments. **** indicates p-value < 0.0001 compared to untreated (by t-test). Scale bars in micrographs indicate 10 μm. See also Figure 4 – figure supplement 1.

While vesicle-mediated transport is the major pathway by which proteins move from the ER and onward through the secretory pathway, alternative modes of removing protein from the ER exist, in particular during ER stress. Recent evidence indicates that the ER can undergo autophagy under various conditions, including acute ER stress(Smith et al., 2018). To evaluate the possibility that EMDΔ95-99-GFP could be engulfed and removed from the NE and ER by autophagosomes, we tested the ability of the PI3K inhibitor KU55933 to reverse EMDΔ95-99-GFP loss. PI3K signaling promotes the formation of isolation membranes that engulf autophagic cargo (Farkas, Daugaard, & Jäättelä, 2011; Klionsky et al., 2016). We observed that cotreatment with KU55933 during acute ER stress could not prevent loss of EMDΔ95-99-GFP from the NE/ER (Fig. 5A-C), in contrast to the ability of BFA treatment to rescue EMD loss. This indicates that vesicle-mediated transport to the Golgi and not autophagic engulfment mediates EMDΔ95-99-GFP's exit from the ER during stress.

Proteins in post-ER compartments can be degraded by vesicle-mediated traffic to the lysosome(Saftig & Klumperman, 2009). To investigate whether the lysosome was the eventual destination of EMDΔ95-99-GFP after ER export, we co-incubated cells expressing EMDΔ95-99-GFP with THG and bafilomycin A1 (Baf A1), which impairs

375 lysosome acidification and thus slows protein degradative processes within lysosomes.

Figure 5. Mutant emerin trafficking is dependent on lysosomal but not autophagosomal function.

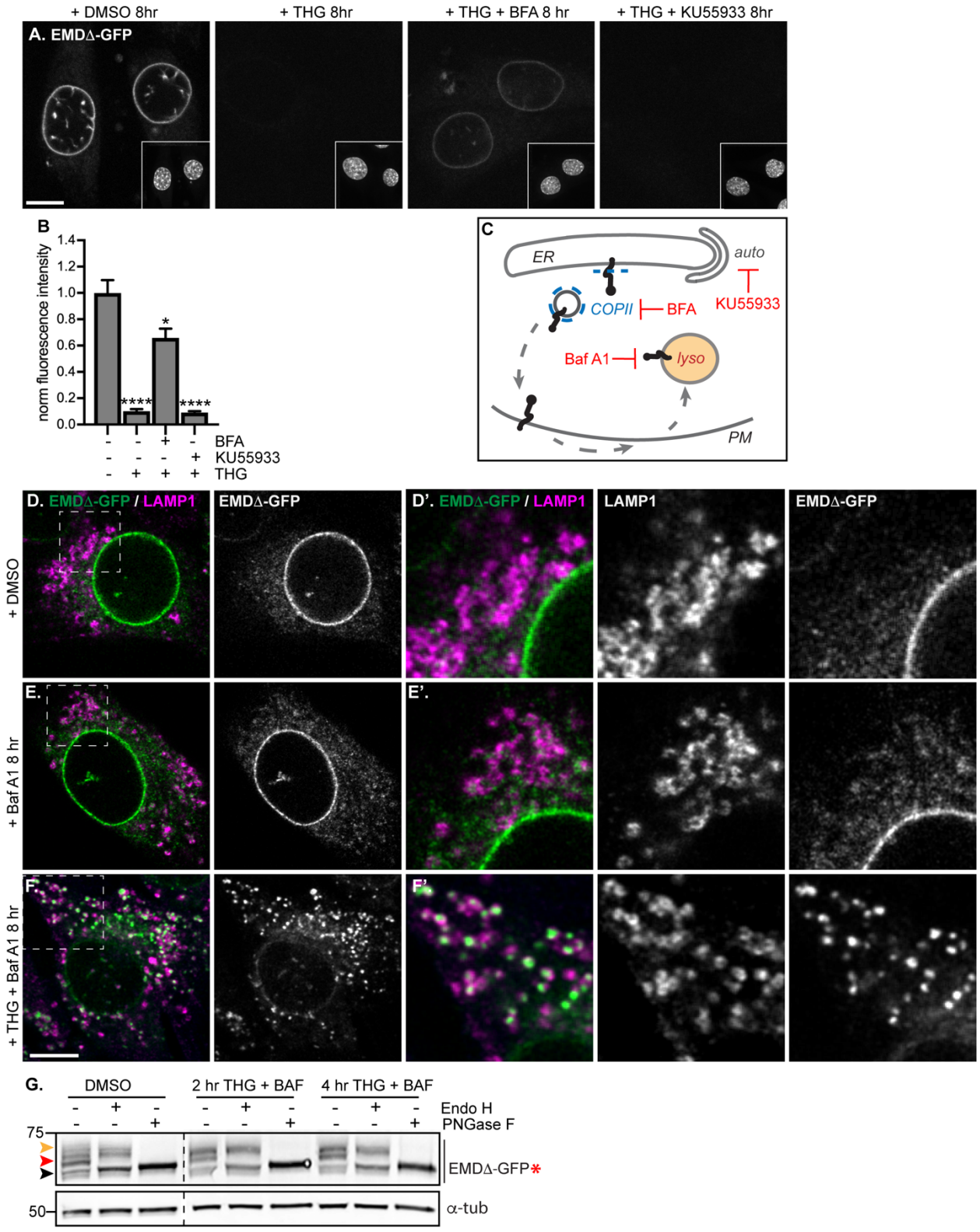

376

Figure 5. Mutant emerin trafficking is dependent on lysosomal but not autophagosomal function. (A) Representative confocal slices of cells stably expressing EMDΔ-GFP after 8 hours of treatment with DMSO vehicle control, THG, co-treatment with THG and BFA, or co-treatment with THG and KU55933. Insets show nuclei in the same field of view stained with Hoechst. (B) Quantification of NE-localized GFP fluorescence intensity in maximum intensity projections of confocal z series acquired across the conditions shown in (A). Columns indicate average and error bars indicate SEM for N > 56 cells from 3 independent experiments. **** indicates p-value < 0.0001 compared to untreated (by t-test). (C) Diagram of processes perturbed by KU55933, BFA, and Baf A1 treatment. (D-F) Representative confocal slices of C2C12 cells stably expressing EMDΔ-GFP and costained for LAMP1 after treatment with DMSO vehicle control (D), Baf A1 (E), or co-treatment with THG and Baf A1 (F) for the indicated times. (D'-F') Insets show GFP-LAMP1 colocalization within ~15 μm field of view demarcated by dashed rectangles in (D-F). (G) Analysis of EMDΔ-GFP* glycosylation state in cells subjected to treatment with DMSO vehicle control or THG and Baf A1 cotreatments for the times indicated. Red arrowhead indicates EndoH-sensitive glycosylated state of EMDΔ-GFP*; orange arrowhead indicates EndoH-resistant states of EMDΔ-GFP*; black arrowhead indicates deglycosylated EMDΔ-GFP*. α-tubulin shown as loading control. Numbers to left of blots indicate molecular weights in kDa. Scale bars in micrographs indicate 10 μm.

Under these conditions, we observed complete translocation of EMDΔ95-99-GFP out of the NE and ER and into numerous vesicles that are decorated with the lysosomal marker LAMP1 (Fig. 5F). Notably, bafilomycin A1 alone did not trap EMDΔ95-99-GFP in lysosomes (Fig. 5E), indicating that ER stress potentiates exit from the NE/ER and lysosomal accumulation. This indicates that the eventual destination of EMDΔ95-99-GFP after export from the NE/ER network is the lysosome.

If EMDΔ95-99 arrives at the lysosome by trafficking through the secretory pathway, this should be accompanied by the accumulation of Endo H-resistant N-glycosylation modifications on our engineered reporter EMDΔ95-99-GFP*. Indeed, we observe that the majority of EMDΔ95-99-GFP* exists as an Endo H-sensitive species in unperturbed cells (Fig. 5G, red arrowhead), but shifts progressively to a higher molecular weight, Endo H-resistant state over 2 to 4 hours of co-treatment with THG and Baf A1 (Fig. 5G, orange arrowhead). This indicates that EMDΔ95-99 traverses the secretory pathway before being delivered to the lysosome.

Emerin transiently accesses the plasma membrane during ER stress

A possible route from the early secretory pathway to the lysosome could involve anterograde transport following the "bulk flow" of the secretory pathway, through the

396 Golgi and into vesicles destined for the plasma membrane (PM). There, mislocalized
397 proteins may be selectively endocytosed and trafficked to lysosomes for degradation
398 through retrograde transport(Saftig & Klumperman, 2009). To explore this possibility, we
399 performed antibody uptake assays in cells expressing EMDΔ95-99-GFP under
400 homeostatic or stressed conditions. EMD is a tail-anchored protein with its final C-
401 terminal amino acids facing the ER lumen; the C-terminal GFP tag will thus face the
402 extracellular space if EMDΔ95-99-GFP accesses the PM (Fig. 6A). We tested whether
403 EMDΔ95-99's GFP tag is accessible to an anti-GFP antibody applied to the surface of
404 intact cells. In untreated cells, a small amount of EMDΔ95-99-GFP (Fig. 6B-D) is
405 accessible to an anti-GFP antibody, but not to an anti-myc antibody, indicating that
406 EMDΔ95-99 is not completely restricted to intracellular membrane compartments under
407 homeostatic conditions. Importantly, the signal from the anti-GFP antibody is specific to
408 cells that express a GFP fusion protein (Fig. 6D-E). Upon induction of ER stress by
409 THG, the amount of PM-accessible EMDΔ95-99-GFP rapidly increases within 2-4
410 hours, and begins to taper off within 6 hours. This implies that ER stress induces the
411 export of EMDΔ95-99-GFP from the NE/ER to the PM as well as its internalization.
412 Importantly, the GFP antibody signal is visible within intracellular puncta, consistent with
413 EMDΔ95-99-GFP:antibody conjugates being rapidly internalized into vesicles after PM
414 delivery. Based on the timescale when the levels of EMDΔ95-99-GFP begin to
415 significantly decrease at the NE (Fig. 3E-F), increase in the Golgi (Fig. 4A-D), transit
416 through the PM (Fig. 6) and accumulate in lysosomes (Fig. 5F), we infer that EMDΔ95-
417 99-GFP is transported through the secretory pathway to the PM, then internalized and
418 delivered to lysosomes for degradation.

Figure 6. Emerin traffics through the plasma membrane upon ER stress

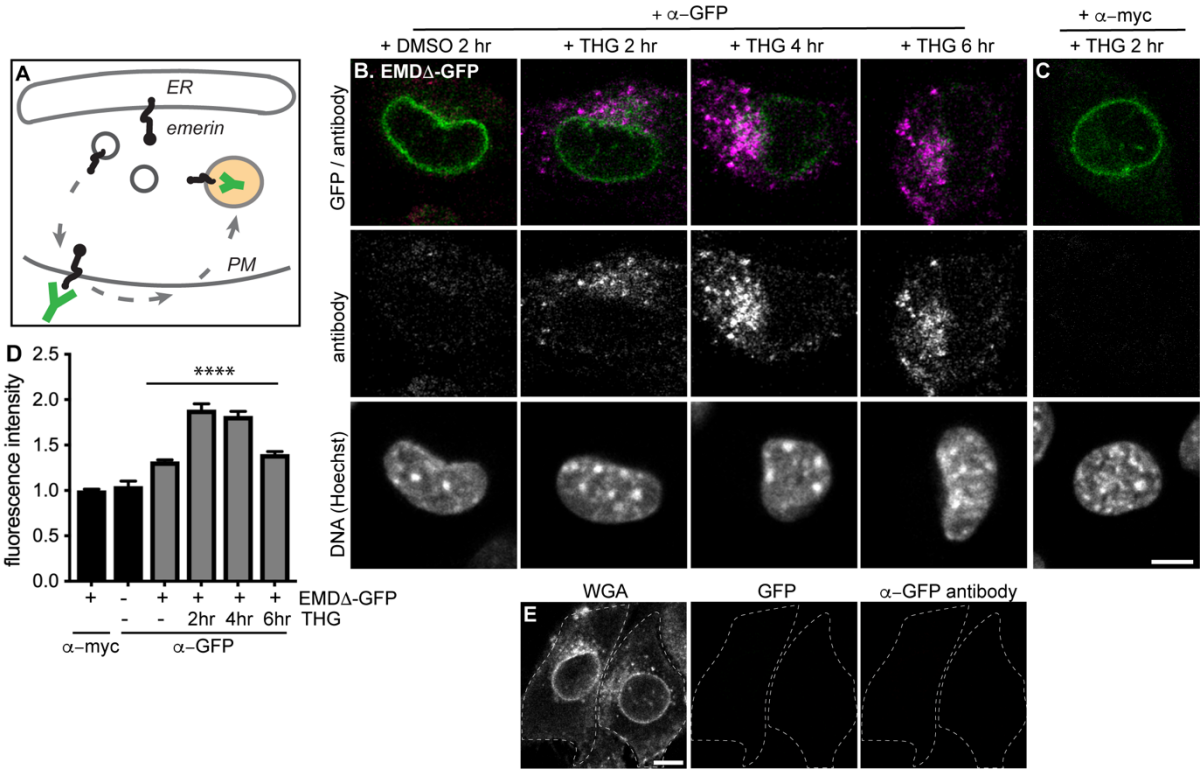

Figure 6. Mutant emerin traffics through the plasma membrane upon ER stress. (A) Schematic of antibody uptake assay experimental design. If emerin accesses the plasma membrane (PM), it will be detected by anti-GFP antibody (green), which will bind the surface-exposed GFP tag. (B) Uptake of anti-GFP antibody (magenta) by cells stably expressing EMDΔ-GFP and treated with DMSO vehicle control or THG for 2, 4, or 6 hours. Cells were incubated with anti-GFP antibody for the final hour of these treatment periods before fixation and imaging. (C) Control demonstrating lack of uptake of anti-myc antibody by cells stably expressing EMDΔ-GFP and treated with THG for 2 hours. (D) Quantification of internalized antibody signal in EMDΔ-GFP expressing cells. Columns indicate average and error bars indicate SEM for N > 235 cells from 3 independent experiments. **** indicates p-value < 0.0001 (t-test) compared to untreated. (E) Control demonstrating lack of uptake of anti-GFP antibody by untreated C2C12 cells that do not express a GFP fusion protein. WGA is used to define cell boundaries. All images were acquired using the same laser power and detector gain settings. Scale bars in micrographs indicate 10 μm. See also Figure 6 – figure supplement 1.

Other INM proteins do not undergo stress-dependent clearance

Our findings indicate that EMDΔ95-99 is subject to proteasome-dependent turnover at the INM (Fig. 2G-H; Fig. 3A-B), but can also be rapidly removed from the INM and ER membrane network and targeted for degradation during ER stress. This raises the possibility that additional INM proteins are susceptible to stress-dependent degradation.

427 To address this, we tested the response of additional INM proteins to ER stress
428 induction by THG, to ER export blockage by BFA, and to lysosomal maturation
429 blockage by Baf A1. We selected proteins with distinct topologies and half-lives,
430 including the long-lived polytopic INM protein nurim and the less stable single-pass
431 transmembrane protein Sun2 (see Fig. 1H, Table S5). Prolonged treatment with THG
432 modestly decreased nurim protein levels and significantly decreased Sun2 protein
433 levels (Fig. 7A-B, D), likely as a consequence of translational inhibition caused by ER
434 stress(Harding, Zhang, & Ron, 1999). Consistent with this interpretation, the sensitivity
435 of these two proteins tracks with the relative differences in their half-lives (Table S5);
436 nurim has a half-life of ~9 days, while Sun2 has a half-life of ~3 days in non-dividing
437 cells. Importantly, however, co-incubation with THG and BFA had no effect on either the
438 subcellular localization or abundance of nurim or Sun2 (Fig. 7A-B, D), indicating that
439 loss of these proteins is not mediated by ER export. Further, neither protein leaves the
440 NE/ER to accumulate in lysosomes when lysosome acidification is blocked by Baf A1
441 (Fig. 7A', B').
442
443 We next asked whether wild type EMD was also subject to this pathway. Similarly to
444 EMDΔ95-99, NE-localized EMD-GFP decreases when stress is induced by THG, but
445 remains stable when stress induction by THG is accompanied by secretory pathway
446 disruption by BFA (Fig. 7C). ER stress also induces EMD-GFP to enrich in the Golgi
447 (Figure 4 – figure supplement 1) and access the plasma membrane (Figure 6 – figure
448 supplement 1). EMD-GFP also accumulates in perinuclear puncta that are likely
449 lysosomes when cells are co-incubated with THG and Baf A1 (Fig. 7C'). We again
450 engineered an opsin glycosylation site onto the C-terminus of EMD-GFP in order to
451 track movement of EMD through membrane compartments. EMD-WT-GFP* localizes to
452 the NE and responds similarly to ER stress and secretory pathway blockage (Figure 7 –
453 figure supplement 1). As we observed with EMDΔ95-99, EMD-WT-GFP* exists
454 predominantly in an Endo H-sensitive modification state in unstressed cells (Fig. 7E-F,
455 red arrowheads). Higher molecular weight, Endo H-resistant species increase in
456 abundance when cells are coincubated with THG and CHX (Fig. 7E, orange arrowhead)
457 or with THG and Baf A1 (Fig. 7F, orange arrowhead). We thus conclude that wild type

EMD is subject to the same stress-induced lysosomal degradation pathway as EMDΔ95-99. However, when EMD-GFP's response to THG is tracked over time, it is clear that displacement of wild type EMD from the NE proceeds significantly more slowly than displacement of EMDΔ95-99 (Fig. 8B, D). This indicates that stress-dependent trafficking out of the INM is selective to variants of EMD, and that intrinsic features of EMD control its clearance from the NE/ER and targeting into lysosomes.

Figure 7. Emerin, but not other INM proteins, undergoes stress-dependent clearance from the NE/ER.

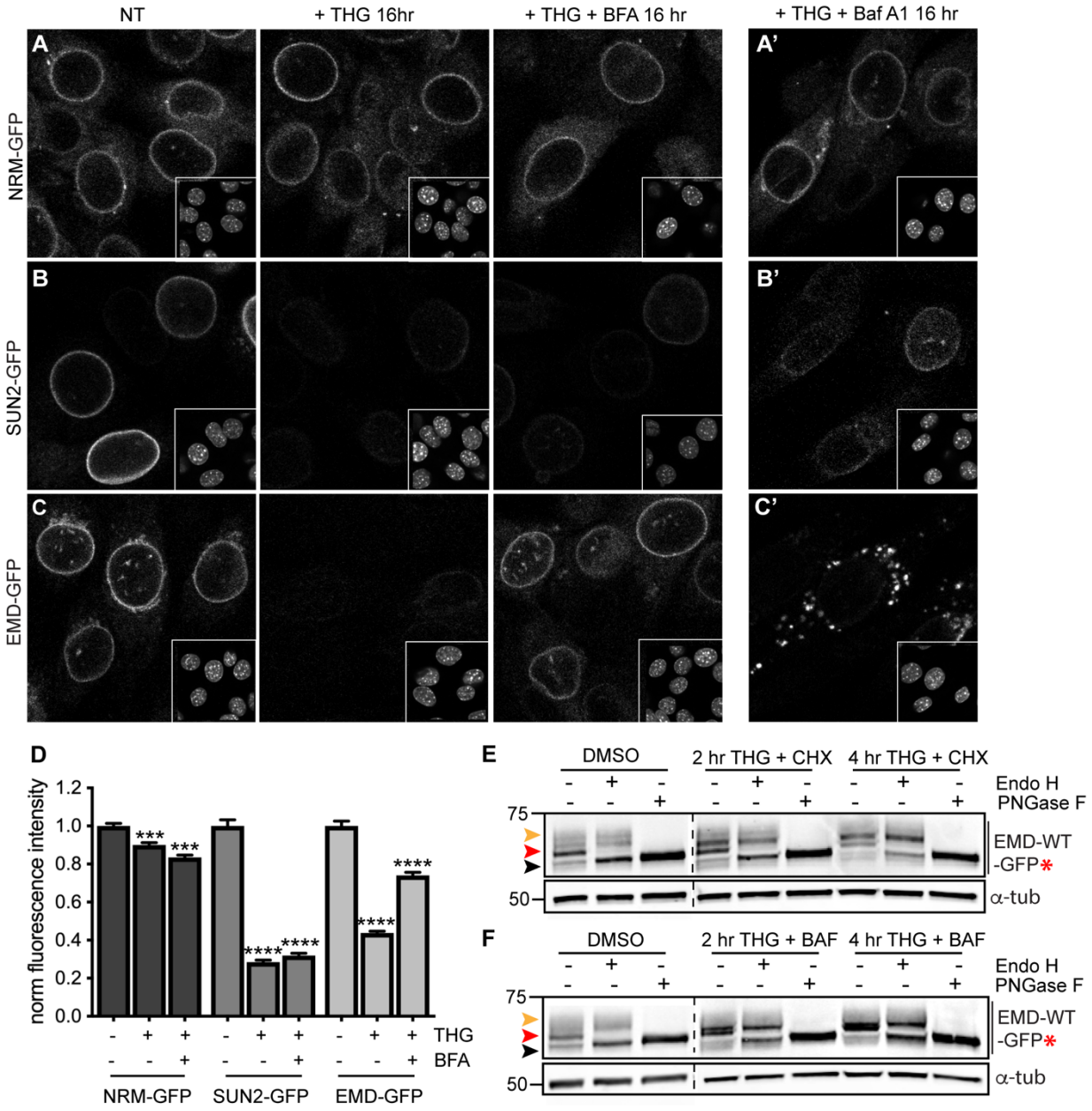

465

Figure 7. Emerin, but not other INM proteins, undergoes stress-dependent clearance from the NE and ER and accesses lysosomes. (A-C) Representative confocal slices of cells stably expressing NRM-GFP (A), Sun2-GFP (B), or EMD-GFP (C) after 16 hours of treatment with DMSO vehicle control, THG, or co-treatment with THG and BFA. Insets show nuclei in the same ~50 µm field of view stained with Hoechst. (A'-C') Representative confocal slices of cells co-treated with THG and Baf A1. All images were acquired using the same laser power and detector gain settings. (D) Quantification of GFP fluorescence intensity at the NE in maximum intensity projections of confocal z series acquired across conditions represented in (A-C). Columns indicate average and error bars indicate SEM for N > 690 cells from 3 independent experiments. **** indicates p-value < 0.0001 compared to untreated (t-test). (E-F) Analysis of EMD-WT-GFP* glycosylation state in cells subjected to treatment with DMSO vehicle control or THG and CHX (E) or THG and Baf A1 (F) cotreatments for the times indicated. Red arrowhead indicates EndoH-sensitive glycosylated state of EMDΔ-GFP*; orange arrowhead indicates EndoH-resistant states of EMDΔ-GFP*; black arrowhead indicates deglycosylated EMDΔ-GFP*. α-tubulin shown as loading control. Numbers to left of blots indicate molecular weights in kDa. Scale bars in micrographs indicate 10 μm. See also Figure 7 – figure supplement 1.

466

467 **A signal within emerin's LEM domain is required for stress-dependent export**

468 Why are EMD variants selectively targeted for stress-dependent clearance from the INM
469 and ER? We considered functional domains that might be involved in responding to ER
470 stress. EMD is a tail-anchored protein with a ~10 amino acid tail that protrudes into the
471 ER lumen (Fig. 3A). This short sequence lacks any known motifs for engaging with
472 proteins within the ER lumen. EMD's nucleoplasmic domain includes an N-terminal LEM
473 domain and an internal lamin A-binding region (Fig. 3A). Emerin relies on lamin A for
474 targeting to the INM(Vaughan et al., 2001) but we noted that in *lmna* -/- MEFs, EMD-
475 GFP remained stably expressed even while mislocalized to the
476 peripheral ER (Figure 8 – figure supplement 2). The small deletion within EMDΔ95-99
477 falls within the lamin A-binding domain, but does not appear to affect the protein's
478 affinity for the lamina as judged by FRAP (Figure 2 – figure supplement 1), even though
479 this variant responds more potently than wild type EMD to ER stress (Fig. 8D). Taken
480 together, these observations indicate that dissociation from the lamina is not sufficient to
481 promote clearance of EMD from the NE/ER membrane system.

482

483 We next evaluated whether interactions mediated by the LEM domain could contribute
484 to stress-dependent EMD export. The LEM domain (Fig. 3A) is a protein fold that binds
485 with high affinity to the soluble nucleoplasmic protein BAF (Lee et al., 2001). We deleted

486 this domain and queried the effects on EMD localization and trafficking. When
487 expressed within unperturbed cells, EMDΔLEM exhibited normal enrichment in the NE
488 (Fig. 8C), consistent with its ability to bind the lamina independently of the LEM domain.
489 However, we observed that this mutant was less responsive than other EMD variants to
490 ER stress induction; NE-localized EMDΔLEM was clearly detectable over several hours
491 of THG treatment and was significantly less sensitive than full-length EMD to ER stress
492 (Fig. 8C-E). We surmise that the eventual loss of EMDΔLEM results from translational
493 inhibition resulting from ER stress(Harding et al., 1999) and degradation by alternative
494 pathways. Consistent with the interpretation that the LEM domain mediates post-ER
495 trafficking, co-incubation of EMDΔLEM-expressing cells with THG and BFA or Baf A1
496 each had no effect on protein levels or localization (Fig. 8F-H). These results suggest
497 that without the LEM domain, EMD does not access post-ER compartments. To directly
498 evaluate this, we generated a glycosylation-reporting variant, EMDΔLEM-GFP*, with a
499 glycosylation consensus site at the lumenal C terminus. In contrast to variants of EMD
500 with an intact LEM domain, EMDΔLEM-GFP* accumulates only Endo H-sensitive
501 modifications and remains equivalently Endo H-sensitive during ER stress and
502 lysosome blockage (Fig. 8I-J, red arrowheads). Altogether, these data indicate that a
503 signal within emerin's LEM domain enables selective export from the ER under stress
504 conditions.

Figure 8. A signal within emerin's LEM domain is required for stress-dependent clearance from the NE/ER

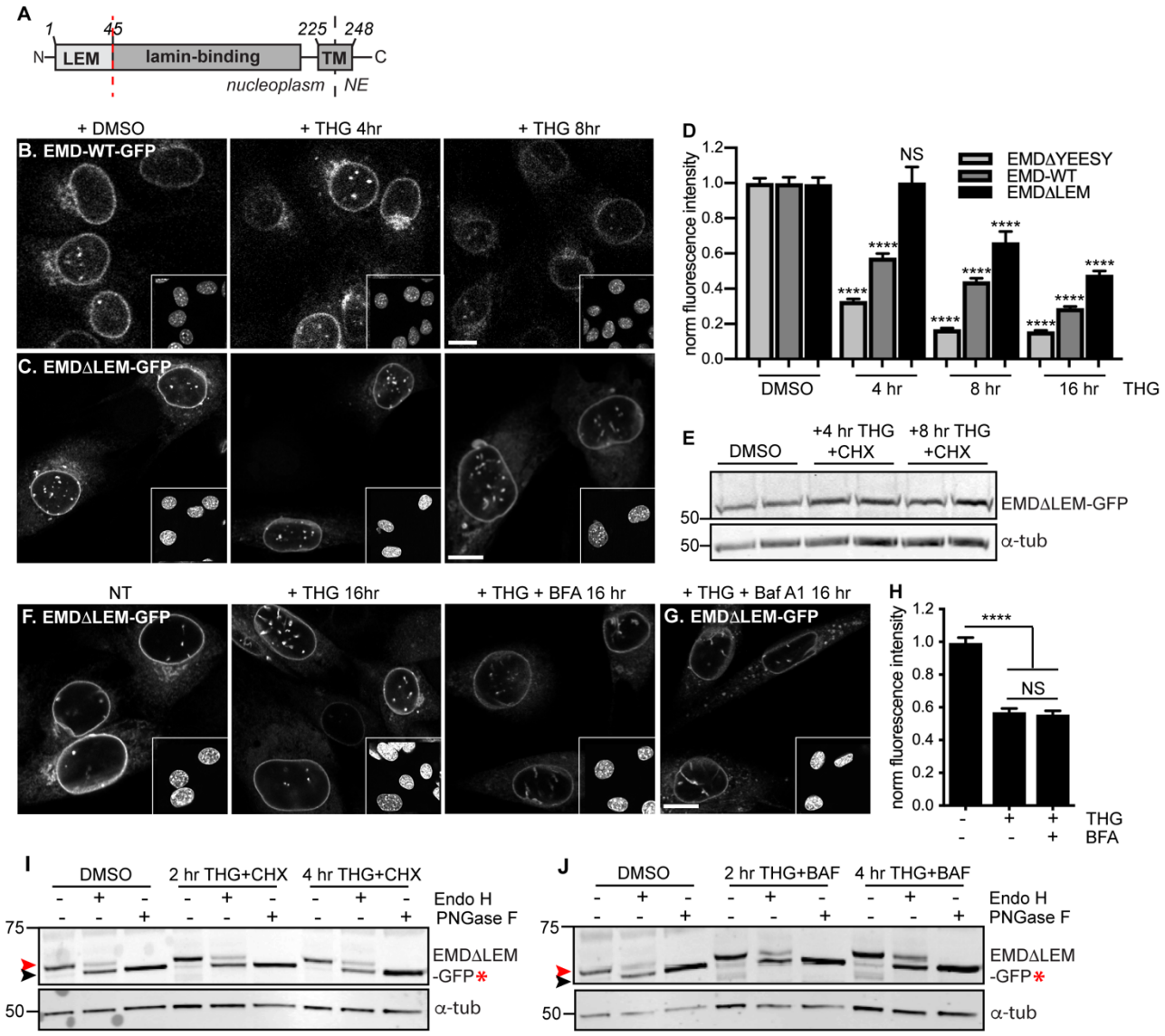

505

Figure 8. A signal within emerin's LEM domain is required for stress-dependent clearance from the NE and ER (A) Diagram of emerin domain organization with N-terminal LEM domain deletion indicated (amino acids 1-45). (B-C) Representative confocal slices of C2C12 cells stably expressing EMD-WT-GFP (B) or EMD∆LEM-GFP (C) after treatment with DMSO vehicle control or THG for the indicated times. Insets show nuclei in the same ~50 µm field of view stained with Hoechst. (D) Quantification of EMD∆YEESY-GFP (as also shown in Figure 3F), EMD-WT-GFP, and EMD∆LEM-GFP fluorescence intensity at the NE in maximum intensity projections of confocal z series acquired across the timecourse shown in (B-C). Columns indicate average and error bars indicate SEM for N > 146 cells from 3 independent experiments. **** indicates p-value < 0.0001 compared to untreated (t-test). (E) Western blot of EMD∆LEM-GFP in cells treated with DMSO vehicle control or co-treated with THG and CHX for the indicated times. (F-G) Representative confocal slices of C2C12 cells stably expressing EMD∆LEM-GFP after treatment with (F) DMSO vehicle control, THG, THG + BFA, or (G) THG + Baf A1. (H) Quantification of GFP fluorescence intensity at the NE across the conditions shown in (F). Columns indicate average and error bars indicate SEM for N > 776 cells from 3 independent experiments. **** indicates p-value < 0.0001 compared to untreated (t-test). (I-J) Analysis of EMD-∆LEM-GFP* glycosylation state in cells subjected to treatment with DMSO vehicle control or THG and CHX (I) or THG and Baf A1 (J) cotreatments for the times indicated. Red arrowhead indicates EndoH-sensitive glycosylated state of EMD∆LEM-GFP*; black arrowhead indicates deglycosylated EMD∆LEM-GFP*. α-tubulin shown as loading control. Numbers to left of blots indicate molecular weights in kDa. Scale bars in micrographs indicate 10 µm. See also Figure 8 – figure supplement 1 and 2.

506

507 **Discussion**

508 In this work, we applied a dynamic proteomic strategy to define organelle-wide trends in
509 protein turnover across the NE/ER membrane network in mammalian cells. While the
510 INM is separated from the bulk ER by the selective barrier of the NPC, we observe no
511 difference in global protein turnover rates between the ER and INM compartments or
512 any correlation between INM protein size and turnover kinetics. This, along with specific
513 visualization of mature INM proteins by RITE tagging and microscopy (Fig. 2) and
514 previous studies(Tsai et al., 2016), suggests that turnover of INM proteins can be
515 effectively achieved *in situ*.

516

517 Moving forward with the rapidly turned over INM protein EMD as a model substrate for
518 dissecting INM protein turnover, we identified an even less stable, EDMD-linked variant
519 of EMD as an ideal substrate for sensitively probing INM protein turnover pathways. We
520 noted that turnover of maturely folded EMD and EMD∆95-99 exhibits proteasome
521 dependence at the INM (Fig. 2F-H; Fig. 3A), while nascent EMD∆95-99 accumulates in
522 multiple cellular compartments when the proteasome is inhibited (Fig. 3A, fourth panel).

523 Taken together, these observations lead us to infer that mature EMD variants and
524 potentially other INM proteins can be turned over *in situ* at the INM by a pathway that
525 terminates in proteasomal degradation, while immature EMD variants (and potentially
526 other INM proteins) are also subject to co-translational quality control that terminates in
527 proteasomal degradation. As proteasomal inhibition and p97 inhibition each stabilize
528 EMDΔ95-99 (Fig. 3B), we expect that EMDΔ95-99 is an ERAD client under some
529 conditions.
530
531 Surprisingly, however, we also find that EMD can be selectively shunted to an
532 alternative turnover pathway under conditions of acute ER stress. This pathway is
533 rapidly induced by ERAD blockage or by pharmacological induction of acute ER protein
534 folding stress (Fig. 3) and requires ER export (Fig. 3, 4). Notably, changes to EMDΔ95-
535 99 localization and levels are apparent at a timescale shorter than the normal half-life of
536 EMDΔ95-99, within 2-4 hours of ER stress induction. Based on the transient
537 appearance of EMDΔ95-99 at the PM (Fig. 6) and its accumulation in lysosomes (Fig.
538 5), we conclude that EMD transits through the secretory pathway and is then
539 internalized into lysosomes. While our data indicate that a significant proportion of EMD
540 leaves the NE/ER during ER stress, we cannot rule out the possibility that ERAD-
541 mediated degradation of some proportion of EMD takes place within the NE/ER network
542 in parallel to the lysosome-mediated pathway that we have identified. Nonetheless, this
543 dynamic and selective removal of an INM protein is quite surprising and is inconsistent
544 with models of the INM as a terminal depot for its resident proteins.
545
546 Our findings have some intriguing parallels to the fate of a misfolded variant of the GPI-
547 anchored prion protein, PrP, during ER stress (Satpute-Krishnan et al., 2014). PrP is
548 normally targeted to the PM, but a misfolded variant is retained within the ER by
549 persistent association with protein folding chaperones. Similarly to what we observe for
550 an INM protein, ER stress induces the rapid export of misfolded PrP through the
551 secretory pathway, followed by transit through the PM and internalization and delivery to
552 lysosomes for degradation. This mode of clearance has been referred to as rapid ER
553 stress-induced export, or RESET(Satpute-Krishnan et al., 2014).

554

555 There are several notable contrasts between PrP's export from the peripheral ER and
556 EMD's export from the INM and ER. For instance, the topologies of PrP and EMD are
557 quite disparate. As a GPI-anchored protein, misfolded PrP faces the lumen of the ER,
558 and an interaction between PrP and Tmp21, a sorting adaptor for luminal proteins,
559 controls RESET(Satpute-Krishnan et al., 2014). Misfolded PrP remains associated with
560 additional luminal ER-derived proteins during its transit through the secretory pathway,
561 and these associations appear to enable recognition of misfolded PrP at the cell surface
562 for internalization (Zavodszky & Hegde, 2019). In contrast, EMD is a tail-anchored
563 protein, and interactions mediated by EMD's nucleoplasmic-facing LEM domain (Fig. 8)
564 control its stress-dependent clearance. We do not yet know whether EMD remains
565 associated with other proteins as it transits through the secretory pathway, or what role
566 those associations might play in targeting EMD for degradation.
567

568 PrP and EMD also exhibit distinct subcellular localization when not undergoing RESET.
569 Misfolded PrP is retained in the ER network until RESET is initiated, while EMD is
570 enriched in the INM and associated with the nuclear lamina. Importantly, EMD is small
571 enough (~25 kDa) to diffuse freely across the NPC, meaning that it may release INM-
572 localized binding partners and sample the ER with some frequency. This spatial
573 separation between EMD's normal site of enrichment and its site of ER export may
574 explain the longer timescale of RESET for EMD (2-4 hours) compared to ER-localized
575 misfolded PrP (~1 hour) (Satpute-Krishnan et al., 2014).
576

577 Finally, PrP and EMD variants exhibit clear differences in selectivity for the RESET
578 pathway. Only misfolded, ER-retained mutants of PrP are subject to RESET. On the
579 other hand, both wild type EMD (Fig. 7) and a less stable disease-linked variant
580 (EMDΔ95-99) are subject to stress-dependent clearance, although EMDΔ95-99 is more
581 rapidly cleared from the NE and ER. Both EMD variants appear functional until ER
582 stress is induced, as judged by their localization and affinity for the INM (Fig. 3, Figure 2
583 – figure supplement 1). This suggests that clearance of EMD from the NE/ER is not
584 strictly contingent on protein misfolding.

Figure 9. Model.

585 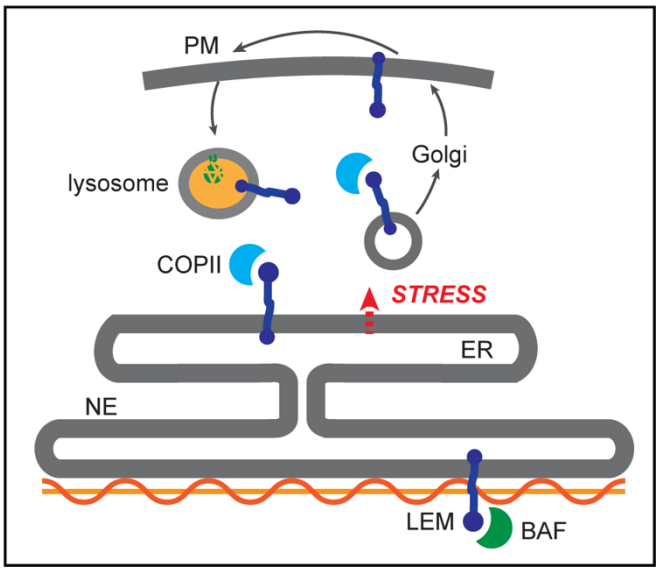

Figure 9. Competition model for emerin sorting via its LEM domain competitively binding to BAF or to the ER export machinery.

586 We find that selective, stress dependent clearance of EMD depends on its 45-amino
587 acid LEM domain. LEM domains bind dynamically to the small soluble protein BAF,
588 which exists in both nuclear and cytoplasmic pools(Shimi et al., 2004). While
589 glycosylation reporters indicate that EMD variants also exit the NE/ER with some
590 frequency under homeostatic conditions (Fig. 3H, Fig. 7E-F), this is completely
591 abolished by deletion of the LEM domain (Fig. 8). One model that could explain the
592 dichotomy between LEM-mediated BAF binding and LEM-mediated ER export is that
593 BAF and ER export-promoting factor(s) bind competitively to the same surface of EMD's
594 LEM domain (Fig. 9). It could be that acute ER stress is relayed to EMD via a structural
595 reorganization or post-translational modification that disrupts the LEM:BAF interface. It
596 is possible that this system could be used to rapidly remove EMD in response to ER
597 stress and potentially other physiological stressors. This could in turn rapidly inhibit the
598 normal functions of EMD at the INM, including participating in mechanosensitive
599 signaling pathways(Guilluy et al., 2014) and contributing to the scaffolding of
600 heterochromatic domains at the nuclear periphery(Demmerle, Koch, & Holaska, 2013).
601 Overall, our findings indicate that the INM can be rapidly remodeled in response to

602 environmental stimuli, and that the function of the INM protein EMD may be dynamically
603 controlled by integration of environmental inputs via its LEM domain.
604
605 Notably, muscular dystrophy and cardiomyopathy diseases are caused by loss-of-
606 function mutations to EMD, many of which further destabilize the protein(Bonne &
607 Quijano-Roy, 2013; Fairley et al., 1999). We find evidence that a muscular dystrophy-
608 linked EMD variant (EMDΔ95-99) is more rapidly degraded under acute stress
609 conditions, suggesting that an overzealous response to ER stress could contribute to
610 the pathogenesis of EDMD. EMD is broadly expressed(Uhlen et al., 2015), but
611 mutations predominantly affect muscle tissues. Intriguingly, skeletal muscle undergoes
612 significant ER stress both during development and during normal function(Deldicque,
613 Hespel, & Francaux, 2012). We speculate that these features of muscle physiology may
614 make muscle-localized EMD mutants especially vulnerable to ER stress-induced
615 degradation.
616

Key Resources Table				
Reagent type (species) or resource	**Designation**	**Source or reference**	**Identifiers**	**Additional information**
gene (*Mus musculus)*	emerin		NCBI RefSeq NM_007927	
Gene (*Mus musculus*)	nurim		NCBI RefSeq NM_134122	
Gene (*Mus musculus*)	Sun2		NCBI RefSeq NM_001205346	
cell line (*Mus musculus)*	C2C12	ATCC	CRL-1772	
cell line (*Homo sapiens*)	U-2-OS	ATCC	HTB-96	

Recombinant DNA reagent (plasmid)	pQCXIB vector	Addgene	Campeau et al., 2009	Retroviral construct for stable expression
Recombinant DNA reagent (plasmid)	Myc/FLAG RITE vector	Toyama et al., JCB 2019		Lentiviral contruct for stable expression of RITE-tagged protein
Recombinant DNA reagent (plasmid)	pQCXIB emerin-GFP	This paper		Retroviral construct for stable expression
Recombinant DNA reagent (plasmid)	pQCXIB emerin-D95-99-GFP	This paper		Retroviral construct for stable expression
Recombinant DNA reagent (plasmid)	pQCXIB emerin-DLEM-GFP	This paper		Retroviral construct for stable expression
Recombinant DNA reagent (plasmid)	pQCXIB emerin-GFP-SSNKTVD	This paper		Retroviral construct for stable expression
Recombinant DNA reagent (plasmid)	pQCXIB emerin-Δ95-99-GFP-SSNKTVD	This paper		Retroviral construct for stable expression
Recombinant DNA reagent (plasmid)	pQCXIB emerin-ΔLEM-GFP-SSNKTVD	This paper		Retroviral construct for stable expression
Recombinant DNA reagent (plasmid)	pQCXIB Sun2-GFP	This paper		Retroviral construct for stable expression

Recombinant DNA reagent (plasmid)	pQCXIB nurim-GFP	This paper		Retroviral construct for stable expression
Recombinant DNA reagent (plasmid)	Emerin-RITE	This paper		Lentiviral contruct for stable expression of RITE-tagged protein
Recombinant DNA reagent (plasmid)	Nurim-RITE	This paper		Lentiviral contruct for stable expression of RITE-tagged protein
Recombinant DNA reagent (plasmid)	Emerin-Δ95-99-RITE	This paper		Lentiviral contruct for stable expression of RITE-tagged protein
Antibody	Rabbit polyclonal anti-emerin	Santa Cruz Biotechnology	Sc-15378	WB (1:1000)
Antibody	GFP	Abcam	ab290	Ab uptake (1:500); WB (1:1000)
Antibody	Mouse monoclonal anti-FLAG	Sigma-Aldrich	F1804	IF (1:1000)
Antibody	Mouse monoclonal anti-Myc	Cell Signaling	2233	IF (1:1000); Ab uptake (1:500)
Antibody	Mouse monoclonal anti-tubulin	Sigma-Aldrich	T5168	WB (1:2500)
Antibody	giantin	BioLegend	PRB-114C	IF (1:1000)

Antibody	LAMP1	Abcam	ab24170	IF(1:100)
Other	Alexa-647 WGA	Life Technologies	W32466	IF (5 ug/ml)
Commercial assay or kit	PNGase F	NEB	P0704	
Commercial assay or kit	Endo H	NEB	P0702	
Chemical compound, drug	Thapsigargin	Thermo Fisher	T7459	Used at 100 nM
Chemical compound, drug	MG132	Cayman Chemical	1211877-36-9	Used at 10 uM
Chemical compound, drug	Bafilomycin A1	BioViotica	BVT-0252	Used at 100 nM
Chemical compound, drug	Brefeldin A	Tocris	1231	Used at 2.5 uM
Chemical compound, drug	Leupeptin	Sigma-Aldrich	L5793	Used at 125 uM
Chemical compound, drug	cycloheximide	Sigma-Aldrich	C-7698	Used at 200 ug/ml
Other	$^{13}C_6$-Lysine	Cambridge Isotopes	CLM-2247	
Other	$^{13}C_6$, $^{15}N_4$-Arginine	Cambridge Isotopes	CNLM-539	
Other	Lysine / arginine free DMEM	Thermo Fisher	88364	
Other	Dialyzed fetal bovine serum	Thermo Fisher	26400044	

Other	Hoechst stain	Molecular Probes	H1399	Used at 10 ug/ml
Recombinant DNA reagent (plasmid)	UBE2G1 miR-E LT3GEPIR	Knott et al., 2014		TGCTGTTGACAGTGAGCGAAAGACAGCTGGCAGAACTCAATAGTGAAGCCACAGATGTATTGAGTTCTGCCAGCTGTCTTCTGCCTACTGCCTCGGA
Recombinant DNA reagent (plasmid)	UBE2G2 miR-E LT3GEPIR	Knott et al., 2014		TGCTGTTGACAGTGAGCGAACCGGGAGCAGTTCTATAAGATAGTGAAGCCACAGATGTATCTTATAGAACTGCTCCCGGTCTGCCTACTGCCTCGGA
Recombinant DNA reagent (plasmid)	UBE2J1 miR-E LT3GEPIR	Knott et al., 2014		TGCTGTTGACAGTGAGCGAAAGGTTGTCTACTTCACCAGATAGTGAAGCCACAGATGTATCTGGTGAAGTAGACAACCTTCTGCCTACTGCCTCGGA
Recombinant DNA reagent (plasmid)	MARCH6 miR-E LT3GEPIR	Knott et al., 2014		TGCTGTTGACAGTGAGCGACTGGATCTTCATTCTTATTTATAGTGAAGCCACAGATGTATAAATAAGAATGAAGATCCAGCTGCCTACTGCCTCGGA
Software, algorithm	Fiji	https://fiji.sc/		
Software, algorithm	RStudio	https://rstudio.com/		

Materials and Methods

620 **SILAC labeling**

621 SILAC labeling was performed as a pulse-chase(Ong & Mann, 2007). Proliferating
622 C2C12 mouse myoblasts were subcultured for >5 population doublings in culture
623 medium containing stable heavy isotopes of lysine and arginine ($^{13}C_6$-Lysine, $^{13}C_6$, $^{15}N_4$-
624 Arginine) to completely label the cellular proteome. Cells were grown in SILAC-
625 formulated DMEM lacking lysine and arginine and supplemented with 20% dialyzed
626 FBS, penicillin/streptomycin, and SILAC amino acids. Complete label incorporation was
627 verified by LC-MS/MS. Myoblasts were then grown to confluency and switched to
628 differentiation medium containing heavy isotopes for 5 days to induce myotube
629 differentiation. Differentiation medium contained SILAC DMEM, 2% dialyzed FBS,
630 penicillin/streptomycin, and SILAC amino acids. Media was refreshed every other day.
631 After differentiation, the mature myotube culture was switched to low serum
632 differentiation medium containing the normal isotopes of lysine and arginine: $^{12}C_6$-
633 Lysine, $^{12}C_6$, $^{14}N_4$-Arginine for 1-3 days.

634 Crude nuclear extracts were prepared similarly to previous work(Buchwalter & Hetzer,
635 2017; Schirmer et al., 2003). Cells were harvested by scraping into PBS, then swollen in
636 hypotonic lysis buffer (10 mM potassium acetate, 20 mM Tris acetate pH 7.5, 0.5 mM
637 DTT, 1.5 mM MgCl2, and protease inhibitors), followed by mechanical lysis through a
638 25-gauge needle and syringe. The nuclei were pelleted and the supernatant (containing
639 cytosol) was decanted. Nuclei were then resuspended in buffer containing 10 mM Tris
640 pH 8.0, 10% sucrose, 1 mM DTT, 0.1 mM MgCl2, 20 ug/ml DNase I, and 1 ug/ml
641 RNase I. After nuclease treatment, nuclei were layered on top of a 30% sucrose
642 cushion and pelleted. Crude nuclei were then extracted in 10 mM Tris pH 8, 1% n-octyl
643 glucoside, 400 mM NaCl, and 1 mM DTT, and extracts and pellets were prepared
644 separately for liquid chromatography-mass spectrometry.

645

646 **LC-MS/MS**

647 Samples were denatured in 8M urea/100 mM TEAB, pH 8.5; reduced with TCEP;
648 alkylated with chloroacetamide; and digested overnight with trypsin. Digestion was
649 quenched with 5% formic acid. Detergent was removed from pulse-labeled SILAC
650 samples with SCX tips (EMD Millipore). Samples were run on a Thermo Orbitrap Fusion

651 Tribrid MS/MS with CID fragmentation. The digest was injected directly onto a 30 cm,
652 75 um ID column packed with BEH 1.7 um C18 resin. Samples were separated at a flow
653 rate of 200 nl/min on a nLC 1000. Buffer A and B were 0.1% formic acid in water and
654 acetonitrile, respectively. A gradient of 1-25% B over 160 min, an increase to 35% B
655 over 60 min, an increase to 90% B over another 10 min and a hold at 90%B for a final
656 10 min of washing was used for a total run time of 240 min. The column was re-
657 equilibrated with 20 ul of buffer A prior to the injection of sample. Peptides were eluted
658 directly from the tip of the column and nanosprayed into the mass spectrometer by
659 application of 2.5 kV voltage at the back of the column. The Orbitrap Fusion was
660 operated in data dependent mode. Full MS1 scans were collected in the Orbitrap at
661 120K resolution with a mass range of 400 to 1500 m/z and an AGC target of 4e. The
662 cycle time was set to 3 s, and within this 3 s the most abundant ions per scan were
663 selected for CID MS/MS in the ion trap with an AGC target of 1e and minimum intensity
664 of 5000. Maximum fill times were set to 50 ms and 100 ms for MS and MS/MS scans,
665 respectively. Quadrupole isolation at 1.6 m/z was used, monoisotopic precursor
666 selection was enabled, charge states of 2-7 were selected and dynamic exclusion was
667 used with an exclusion duration of 5 s.
668
669 **Analysis of proteomic data**
670 Peptide and protein identification, quantification, and analysis were performed with
671 Integrated Proteomics Pipeline (IP2) (Integrated Proteomics Applications;
672 www.integratedproteomics.com). Tandem mass spectra were extracted from raw files
673 using RawConverter(He, Diedrich, Chu, & Yates, 2015) and searched with
674 ProLUCID(Xu et al., 2015) against the mouse UniProt database (ID). The search space
675 included all fully tryptic and half-tryptic peptide candidates. Carbamidomethylation on
676 cysteine was allowed as a static modification. Data were searched with 50 ppm
677 precursor ion tolerance and 600 ppm fragment ion tolerance. Data were filtered to 10
678 ppm precursor ion tolerance post-search. Identified proteins were filtered using
679 DTASelect(Tabb, McDonald, & Yates, 2002) and utilizing a target-decoy database
680 strategy to control the false discovery rate to 1% at the protein level.

681 Census2(Park et al., 2014) was used for quantitative analysis of SILAC-labeled
682 peptides. Peptides were subjected to stringent quality control criteria before inclusion in
683 half-life determination analyses. Firstly, any peptide with a profile score < 0.8 was
684 discarded. Secondly, peptides were filtered based on the extent of correlation between
685 the heavy and light chromatograms, which is quantified as a regression score in
686 Census. Peptides with extreme area ratios (less than 0.111 or greater than 9) were
687 retained only if their regression score was > 0. Peptides with intermediate area ratios
688 (between 0.111 and 9) were retained only if their regression score was > 0.8.
689
690 **Half-life calculation**
691 For estimation of protein half-lives, we restricted our analysis to peptides that were
692 detected in at least 3 timepoints. 1685 proteins passed this criterion with at least 1
693 peptide; individual peptides and protein-level data are reported in Tables S1 and S2,
694 respectively. Area ratio values were transformed into % old values using the following
695 equation:
696
697 $\%old = 100^* (1/(1+ AR))$
698
699 And individual peptides were fit to a line corresponding to the following equation:
700
701 $Ln(\%old) = kt + a$
702
703 Individual peptide fits with $r^2 > 0.8$ and values of $k < 0$ were retained for protein-level
704 estimation of half-life. The slope of the fit for all peptides detected were averaged to
705 produce an average value and standard deviation at the protein level. These average
706 slope values were converted to half-life estimates using the equation below.
707
708 $T1/2 = - \ln(2)/k$
709
710 These values are reported in Table S3 for 1677 proteins. While calculated half-lives
711 range from ~0.33 days to ~30 days, we note that half-lives at either extreme should be

712 considered rough estimates of protein stability. For illustration, we have included
713 example fits for proteins in Figure S1 with predicted half-lives of 0.5 day, 1 day, 2 days,
714 4 days, 8 days, and 16 days. Linear regression predicts half-life well under conditions
715 where a line can be fit with high fidelity and a non-zero slope is detectable. We note the
716 good performance and clear distinctions in slope for proteins with predicted half-lives
717 ranging from 1 to 8 days, and observed more frequent deviations in linearity at the low
718 extreme (predicted T1/2 <1 day) and slopes approaching zero at the high extreme
719 (predicted T1/2 > 8 days). We expect that these factors limit the precision of half-life
720 determination below 1 day and above 8 days from a 3-day timecourse. Shorter or longer
721 timecourses would be required to investigate turnover at these timescales.
722
723 The TMHMM server(Krogh, Larsson, Heijne, & Sonnhammer, 2001) was used to define
724 the positions of transmembrane domains in INM proteins and infer extraluminal domain
725 sequences.
726
727 **Plasmid construction**
728 All emerin constructs are based on the emerin sequence from mouse (Uniprot ID
729 O08579); all nurim constructs based on the nurim sequence from mouse (Uniprot ID
730 Q8VC65); and all Sun2 constructs based on the Sun2 sequence from mouse (Uniprot
731 ID Q8BJS4). Emerin, Sun2, and nurim were each C-terminally tagged with GFP by
732 stitching PCR(Heckman & Pease, 2007), where each open reading frame was amplified
733 with the start codon included and the stop codon omitted, while GFP was amplified with
734 its start codon omitted and stop codon included. Primersets were designed with
735 overhangs including homology between each ORF and GFP, so that a second round of
736 PCR with flanking primers and the first two PCR products used as templates generates
737 an ORF-GFP fusion. EMDΔ95-99 was generated by Quickchange mutagenesis of the
738 emerin-GFP sequence followed by sequence verification. EMDΔLEM-GFP was
739 constructed by stitching PCR of emerin nucleic acid sequence 136-777 corresponding
740 to residues 46-258 of emerin protein with the stop codon omitted. A new ATG start
741 codon was introduced by PCR, and the C-terminal GFP tag introduced by stitching
742 PCR. All ORFs were introduced into the pQCXIB vector(Campeau et al., 2009) for

743 retroviral delivery and constitutive expression under a CMV promoter by Gateway
744 cloning.
745
746 INM-RITE tag plasmids were constructed as described in(Toyama et al., 2019). ORFs
747 of interest were introduced into the FLAG/myc-RITE or myc/FLAG-RITE plasmid
748 backbones, then the entire ORF-RITE construct was amplified and recombined into a
749 pDONR207 Gateway entry vector, followed by recombination into the pQCXIB retroviral
750 vector for constitutive mammalian expression.
751
752 Glycosylation reporter plasmids were constructed by introducing a 21 base-pair
753 sequence encoding the glycosylation acceptor site SSNKTVD within a 3' PCR primer for
754 amplification of EMD-WT-GFP, EMD∆YEESY-GFP, and EMD∆LEM-GFP. The resulting
755 PCR product was inserted into the pQCXIB vector by Gateway cloning. Sequence
756 verified clones were used for stable cell line generation.
757
758 UBE2G1, UBE2G2, UBE2J1, and MARCH6 miR-E inducible RNAi plasmids were
759 constructed as described in(Fellmann et al., 2013). Validated shRNA sequences with
760 the highest score for targeting mouse UBE2G1, UBE2G2, UBE2J1, and MARCH6 were
761 selected from the shERWOOD database (www.sherwood.cshl.edu), and ~100 bp
762 oligonucleotides with the corresponding sequence were synthesized. This sequence
763 was amplified by PCR using degenerate primers with XhoI and EcoRI restriction sites.
764 The PCR was digested with XhoI and EcoRI, gel purified, and ligated into the
765 LT3GEPIR lentiviral vector for doxycycline-inducible RNAi expression with GFP reporter
766 fluorescence. The LT3GEPIR vector was the kind gift of Johannes Zuber.
767
768 **Cell line generation**
769 GFP-tagged cell lines were generated in C2C12 mouse myoblasts. Low-passage
770 C2C12 cells were obtained from ATCC, and identity was validated by a functional
771 assay: cells were grown to confluency, switched to low serum medium for several days,
772 and evaluated for the formation of multinucleated myotubes. Parallel cultures of C2C12
773 cells were infected with virus encoding GFP fusion proteins. 293T cells were transfected

774 with delivery vectors and viral packaging vectors for retroviral or lentiviral production.
775 Conditioned media were collected 48-72 hours after transfection and applied to low-
776 passage C2C12 cells in the presence of polybrene. Integrated clones were selected
777 using the relevant antibiotic selections for each vector backbone. Fluorescent cell
778 populations were isolated by FACS. The resulting stable GFP-expressing C2C12 cell
779 lines were tested to verify the absence of mycoplasma contamination. miR-E RNAi cell
780 lines were generated in U2OS cells. U2OS cells were obtained from ATCC and were
781 periodically tested for mycoplasma contamination. EMD∆95-99-GFP was introduced by
782 retroviral infection and FACS sorted as described above. miR-E RNAi expression
783 vectors were then introduced into these stable cell lines by lentiviral infection.
784

785 **RITE tag switching**

786 RITE tag switching experiments were performed in quiescent C2C12 cells stably
787 expressing RITE-tagged INM proteins. C2C12s were grown in Ibidi chamber slides and
788 induced to enter quiescence as previously described(K. Zhang, Sha, & Harter, 2010) by
789 growing C2C12 myoblasts to ~75% confluence, washing twice in warm PBS, and
790 switching to quiescent medium (DMEM without methionine, 2% FBS, and pen-strep).
791 Cells were maintained in quiescent medium for 3 days with media changes every other
792 day before initiation of RITE timecourses. To induce tag exchange, concentrated
793 adenovirus expressing Cre recombinase was added to the culture medium. Tag
794 switching was initiated at the indicated timepoints such that the entire slide containing
795 all time points could be fixed, stained, imaged, and quantified in parallel. To quantify
796 loss of “old” RITE-tagged protein over time, intensity per unit area of the “old” tag was
797 quantified across all conditions. Background measurements were taken from cell-free
798 regions of the imaging dish and subtracted from all signals as a background correction.
799 All signals were then normalized to the day 0 timepoint (no tag switch).
800

801 **Antibody uptake assays**

802 For antibody uptake assays, cells were pre-treated with drugs for the indicated times,
803 then incubated in medium containing antibody, drug, and 125 μM leupeptin for 1 hour
804 before fixation in paraformaldehyde and staining. Cells were stained with Alexa Fluor-

805 conjugated secondary antibody to visualize internalized primary antibody:GFP
806 conjugates. Cell surfaces were stained with Alexa Fluor-conjugated WGA; the WGA
807 signal was used as a guide for outlining individual cells and quantifying internalized
808 antibody fluorescence.
809
810 **Preparation of protein lysates and Western blotting**
811 Cells were washed in PBS, then lysed directly in plates in PBS lysis buffer (PBS
812 supplemented with 1% Triton-X-100, 0.1% SDS, and protease inhibitors). Cells were
813 further lysed by passage through a 25-gauge needle. Protein concentrations were
814 quantified by BCA assay, and ~20 ug of total protein was loaded per lane of 4-12%
815 gradient gels (Invitrogen). Blots were incubated with emerin antibody (1:1000) or alpha-
816 tubulin antibody (1:5000) followed by IR Dye-conjugated secondary antibodies (1:5000)
817 for multiplexed detection on the Odyssey imaging system.
818
819 **Microscopy and image analysis**
820 Cells were grown in Ibidi culture chambers, treated as indicated, and fixed in 4% PFA
821 for 5 minutes, then permeabilized in IF buffer (PBS, 0.1% Tx100, 0.02% SDS, 10 mg/ml
822 BSA) before staining with Hoechst DNA dye. Wells were rinsed in PBS before imaging
823 on a Zeiss LSM 710 scanning confocal microscope with a 63 x 1.4 NA objective.
824 Images shown are single confocal slices. All image quantification was performed on
825 maximum intensity projections of z-series with ImageJ. To quantify NE-localized protein
826 levels, the DNA stain was used as a mask, and all GFP fluorescence within that mask
827 was quantified.
828
829 For lysosomal staining, cells were prepared as described(Castellano et al., 2017) with
830 the following modifications. Following fixation in 4% PFA for 5 minutes, cells were rinsed
831 in PBS, then permeabilized in freshly prepared 0.1% digitonin in PBS for 10 minutes at
832 4C. Cells were rinsed again in PBS, then blocked in 2% goat serum in PBS for 30
833 minutes before staining with LAMP1 antibody (1:100 in 2% goat serum) for 1-2 hours at
834 RT. Cells were rinsed again in PBS, then stained with Alexa Fluor-conjugated
835 secondary antibody and Hoechst DNA stain for 1 hour at RT.

836

837 **References**

838 Albert, S., Schaffer, M., Beck, F., Mosalaganti, S., Asano, S., Thomas, H. F., et al.
839 (2017). Proteasomes tether to two distinct sites at the nuclear pore complex.
840 *Proceedings of the National Academy of Sciences*, *114*(52), 13726–13731.
841 http://doi.org/10.1073/pnas.1716305114

842 Barlowe, C. K., & Miller, E. A. (2013). Secretory Protein Biogenesis and Traffic in the
843 Early Secretory Pathway. *Genetics*, *193*(2), 383–410.
844 http://doi.org/10.1534/genetics.112.142810

845 Boni, A., Politi, A. Z., Strnad, P., Xiang, W., Hossain, M. J., & Ellenberg, J. (2015). Live
846 imaging and modeling of inner nuclear membrane targeting reveals its molecular
847 requirements in mammalian cells. *The Journal of Cell Biology*, *209*(5), 705–720.
848 http://doi.org/10.1083/jcb.201409133

849 Bonne, G., & Quijano-Roy, S. (2013). Emery-Dreifuss muscular dystrophy,
850 laminopathies, and other nuclear envelopathies. *Pediatric Neurology, Part III* (1st
851 ed., Vol. 113, pp. 1367–1376). Elsevier B.V. http://doi.org/10.1016/B978-0-444-
852 59565-2.00007-1

853 Brachner, A., & Foisner, R. (2011). Evolvement of LEM proteins as chromatin tethers at
854 the nuclear periphery. *Biochemical Society Transactions*, *39*(6), 1735–1741.
855 http://doi.org/10.1042/BST20110724

856 Buchwalter, A., & Hetzer, M. W. (2017). Nucleolar expansion and elevated protein
857 translation in premature aging. *Nature Communications*, 1–13.
858 http://doi.org/10.1038/s41467-017-00322-z

859 Bulbarelli, A., Sprocati, T., Barberi, M., Pedrazzini, E., & Borgese, N. (2002). Trafficking
860 of tail-anchored proteins: transport from the endoplasmic reticulum to the plasma
861 membrane and sorting between surface domains in polarised epithelial cells.
862 *Journal of Cell Science*, *115*(Pt 8), 1689–1702.

863 Cambridge, S. B., Gnad, F., Nguyen, C., Bermejo, J. L., Krüger, M., & Mann, M. (2011).
864 Systems-wide Proteomic Analysis in Mammalian Cells Reveals Conserved,
865 Functional Protein Turnover. *Journal of Proteome Research*, *10*(12), 5275–5284.
866 http://doi.org/10.1021/pr101183k

867 Campeau, E., Ruhl, V. E., Rodier, F., Smith, C. L., Rahmberg, B. L., Fuss, J. O., et al.
868 (2009). A Versatile Viral System for Expression and Depletion of Proteins in
869 Mammalian Cells. *PLoS ONE*, *4*(8), e6529–18.
870 http://doi.org/10.1371/journal.pone.0006529
871 Castellano, B. M., Thelen, A. M., Moldavski, O., Feltes, M., van der Welle, R. E. N.,
872 Mydock-McGrane, L., et al. (2017). Lysosomal cholesterol activates mTORC1 via an
873 SLC38A9-Niemann-Pick C1 signaling complex. *Science*, *355*(6331), 1306–1311.
874 http://doi.org/10.1126/science.aag1417
875 Chardin, P., & McCormick, F. (1999). Brefeldin A: the advantage of being
876 uncompetitive. *Cell*, *97*(2), 153–155. http://doi.org/10.1016/s0092-8674(00)80724-2
877 Christianson, J. C., Olzmann, J. A., Shaler, T. A., Sowa, M. E., Bennett, E. J., Richter,
878 C. M., Tyler, R. E., Greenblatt, E. J., Harper, J. W., et al. (2011a). Defining human
879 ERAD networks through an integrative mapping strategy. *Nature Publishing Group*,
880 *14*(1), 93–105. http://doi.org/10.1038/ncb2383
881 Christianson, J. C., Olzmann, J. A., Shaler, T. A., Sowa, M. E., Bennett, E. J., Richter,
882 C. M., Tyler, R. E., Greenblatt, E. J., Wade Harper, J., et al. (2011b). Defining
883 human ERAD networks through an integrative mapping strategy. *Nature Cell*
884 *Biology*, *14*(1), 93–105. http://doi.org/10.1038/ncb2383
885 D'Angelo, M. A., Raices, M., Panowski, S. H., & Hetzer, M. W. (2009). Age-Dependent
886 Deterioration of Nuclear Pore Complexes Causes a Loss of Nuclear Integrity in
887 Postmitotic Cells. *Cell*, *136*(2), 284–295. http://doi.org/10.1016/j.cell.2008.11.037
888 Deldicque, L., Hespel, P., & Francaux, M. (2012). Endoplasmic reticulum stress in
889 skeletal muscle: origin and metabolic consequences. *Exercise and Sport Sciences*
890 *Reviews*, *40*(1), 43–49. http://doi.org/10.1097/JES.0b013e3182355e8c
891 Demmerle, J., Koch, A. J., & Holaska, J. M. (2013). Emerin and histone deacetylase 3
892 (HDAC3) cooperatively regulate expression and nuclear positions of MyoD, Myf5,
893 and Pax7 genes during myogenesis. *Chromosome Research*, *21*(8), 765–779.
894 http://doi.org/10.1007/s10577-013-9381-9
895 Deshaies, R. J., & Joazeiro, C. A. P. (2009). RING Domain E3 Ubiquitin Ligases.
896 *Annual Review of Biochemistry*, *78*(1), 399–434.
897 http://doi.org/10.1146/annurev.biochem.78.101807.093809

898 Dörrbaum, A. R., Kochen, L., Langer, J. D., & Schuman, E. M. (2018). Local and global
899 influences on protein turnover in neurons and glia. *eLife*, *7*, 489.
900 http://doi.org/10.7554/eLife.34202
901 Fagioli, C., & Sitia, R. (2001). Glycoprotein Quality Control in the Endoplasmic
902 Reticulum. *Journal of Biological Chemistry*, *276*(16), 12885–12892.
903 http://doi.org/10.1074/jbc.M009603200
904 Fairley, E. A., Kendrick-Jones, J., & Ellis, J. A. (1999). The Emery-Dreifuss muscular
905 dystrophy phenotype arises from aberrant targeting and binding of emerin at the
906 inner nuclear membrane. *Journal of Cell Science*, *112 (Pt 15)*, 2571–2582.
907 Farkas, T., Daugaard, M., & Jäättelä, M. (2011). Identification of Small Molecule
908 Inhibitors of Phosphatidylinositol 3-Kinase and Autophagy. *Journal of Biological*
909 *Chemistry*, *286*(45), 38904–38912. http://doi.org/10.1074/jbc.M111.269134
910 Fellmann, C., Hoffmann, T., Sridhar, V., Hopfgartner, B., Muhar, M., Roth, M., et al.
911 (2013). An Optimized microRNA Backbone for Effective Single-Copy RNAi.
912 *CellReports*, *5*(6), 1704–1713. http://doi.org/10.1016/j.celrep.2013.11.020
913 Foresti, O., Ruggiano, A., Hannibal-Bach, H. K., Ejsing, C. S., & Carvalho, P. (2013).
914 Sterol homeostasis requires regulated degradation of squalene monooxygenase by
915 the ubiquitin ligase Doa10/Teb4. *eLife*, *2*, 10189–17.
916 http://doi.org/10.7554/eLife.00953
917 Gao, R., Schellenberg, M. J., Huang, S.-Y. N., Abdelmalak, M., Marchand, C., Nitiss, K.
918 C., et al. (2014). Proteolytic degradation of topoisomerase II (Top2) enables the
919 processing of Top2·DNA and Top2·RNA covalent complexes by tyrosyl-DNA-
920 phosphodiesterase 2 (TDP2). *Journal of Biological Chemistry*, *289*(26), 17960–
921 17969. http://doi.org/10.1074/jbc.M114.565374
922 Guilluy, C., Osborne, L. D., Van Landeghem, L., Sharek, L., Superfine, R., Garcia-Mata,
923 R., & Burridge, K. (2014). Isolated nuclei adapt to force and reveal a
924 mechanotransduction pathway in the nucleus. *Nature Cell Biology*, *16*(4), 376–381.
925 http://doi.org/10.1038/ncb2927
926 Harding, H. P., Zhang, Y., & Ron, D. (1999). Protein translation and folding are coupled
927 by an endoplasmic-reticulum-resident kinase. *Nature*, *397*(6716), 271–274.
928 http://doi.org/10.1038/16729

He, L., Diedrich, J., Chu, Y.-Y., & Yates, J. R., III. (2015). Extracting Accurate Precursor Information for Tandem Mass Spectra by RawConverter. *Analytical Chemistry*, *87*(22), 11361–11367. http://doi.org/10.1021/acs.analchem.5b02721

Heckman, K. L., & Pease, L. R. (2007). Gene splicing and mutagenesis by PCR-driven overlap extension. *Nature Protocols*, *2*(4), 924–932. http://doi.org/10.1038/nprot.2007.132

Hegde, R. S., & Zavodszky, E. (2019). Recognition and Degradation of Mislocalized Proteins in Health and Disease. *Cold Spring Harbor Perspectives in Biology*, a033902–19. http://doi.org/10.1101/cshperspect.a033902

Hofemeister, H., & O'Hare, P. (2005). Analysis of the Localization and Topology of Nurim, a Polytopic Protein Tightly Associated with the Inner Nuclear Membrane. *Journal of Biological Chemistry*, *280*(4), 2512–2521. http://doi.org/10.1074/jbc.M410504200

Katta, S. S., Smoyer, C. J., & Jaspersen, S. L. (2014). Destination: inner nuclear membrane. *Trends in Cell Biology*, *24*(4), 221–229. http://doi.org/10.1016/j.tcb.2013.10.006

Khmelinskii, A., Blaszczak, E., Pantazopoulou, M., Fischer, B., Omnus, D. J., Le Dez, G., Brossard, A., Gunnarsson, A., Barry, J. D., Meurer, M., Kirrmaier, D., Boone, C., Huber, W., Rabut, G., Ljungdahl, P. O., & Knop, M. (2014a). Protein quality control at the inner nuclear membrane. *Nature*, *516*(7531), 410–413. http://doi.org/10.1038/nature14096

Khmelinskii, A., Blaszczak, E., Pantazopoulou, M., Fischer, B., Omnus, D. J., Le Dez, G., Brossard, A., Gunnarsson, A., Barry, J. D., Meurer, M., Kirrmaier, D., Boone, C., Huber, W., Rabut, G., Ljungdahl, P. O., & Knop, M. (2014b). Protein quality control at the inner nuclear membrane. *Nature*, *516*(7531), 410–413. http://doi.org/10.1038/nature14096

Klionsky, D. J., Abdelmohsen, K., Abe, A., Abedin, M. J., Abeliovich, H., Arozena, A. A., et al. (2016). Guidelines for the use and interpretation of assays for monitoring autophagy \(3rd edition\). *Autophagy*, *12*(1), 1–222. http://doi.org/10.1080/15548627.2015.1100356

959 Krogh, A., Larsson, B., Heijne, von, G., & Sonnhammer, E. L. L. (2001). Predicting
960 transmembrane protein topology with a hidden markov model: application to
961 complete genomes11Edited by F. Cohen. *Journal of Molecular Biology*, *305*(3),
962 567–580. http://doi.org/10.1006/jmbi.2000.4315
963 Lee, K. K., Haraguchi, T., Lee, R. S., Koujin, T., Hiraoka, Y., & Wilson, K. L. (2001).
964 Distinct functional domains in emerin bind lamin A and DNA-bridging protein BAF.
965 *Journal of Cell Science*, *114*(Pt 24), 4567–4573.
966 Leto, D. E., Morgens, D. W., Zhang, L., Walczak, C. P., Elias, J. E., Bassik, M. C., &
967 Kopito, R. R. (2019). Genome-wide CRISPR Analysis Identifies Substrate- Specific
968 Conjugation Modules in ER-Associated Degradation. *Molecular Cell*, *73*(2), 377–
969 389.e11. http://doi.org/10.1016/j.molcel.2018.11.015
970 Ong, S.-E., & Mann, M. (2007). A practical recipe for stable isotope labeling by amino
971 acids in cell culture (SILAC). *Nature Protocols*, *1*(6), 2650–2660.
972 http://doi.org/10.1038/nprot.2006.427
973 Park, S. K. R., Aslanian, A., McClatchy, D. B., Han, X., Shah, H., Singh, M., et al.
974 (2014). Census 2: isobaric labeling data analysis. *Bioinformatics (Oxford, England)*,
975 *30*(15), 2208–2209. http://doi.org/10.1093/bioinformatics/btu151
976 Pryszcz, L. P., Huerta-Cepas, J., & Gabaldón, T. (2010). MetaPhOrs: orthology and
977 paralogy predictions from multiple phylogenetic evidence using a consistency-based
978 confidence score. *Nucleic Acids Research*, *39*(5), e32–e32.
979 http://doi.org/10.1093/nar/gkq953
980 Rolls, M. M., Stein, P. A., Taylor, S. S., Ha, E., McKeon, F., & Rapoport, T. A. (1999). A
981 Visual Screen of a Gfp-Fusion Library Identifies a New Type of Nuclear Envelope
982 Membrane Protein. *The Journal of Cell Biology*, *146*(1), 29–44.
983 http://doi.org/10.1083/jcb.146.1.29
984 Ruggiano, A., Foresti, O., & Carvalho, P. (2014). ER-associated degradation: Protein
985 quality control and beyond. *The Journal of Cell Biology*, *204*(6), 869–879.
986 http://doi.org/10.1083/jcb.201312042
987 Saftig, P., & Klumperman, J. (2009). Lysosome biogenesis and lysosomal membrane
988 proteins: trafficking meets function, 1–13. http://doi.org/10.1038/nrm2745

989 Satpute-Krishnan, P., Ajinkya, M., Bhat, S., Itakura, E., Hegde, R. S., & Lippincott-
990 Schwartz, J. (2014). ER Stress-Induced Clearance of Misfolded GPI-Anchored
991 Proteins via the Secretory Pathway. *Cell*, *158*(3), 522–533.
992 http://doi.org/10.1016/j.cell.2014.06.026
993 Schirmer, E. C., Florens, L., Guan, T., Yates, J. R., & Gerace, L. (2003). Nuclear
994 membrane proteins with potential disease links found by subtractive proteomics.
995 *Science*, *301*(5638), 1380–1382. http://doi.org/10.1126/science.1088176
996 Schreiber, K. H., & Kennedy, B. K. (2013). When Lamins Go Bad: Nuclear Structure
997 and Disease. *Cell*, *152*(6), 1365–1375. http://doi.org/10.1016/j.cell.2013.02.015
998 Shimi, T., Koujin, T., Segura-Totten, M., Wilson, K. L., Haraguchi, T., & Hiraoka, Y.
999 (2004). Dynamic interaction between BAF and emerin revealed by FRAP, FLIP, and
1000 FRET analyses in living HeLa cells. *Journal of Structural Biology*, *147*(1), 31–41.
1001 http://doi.org/10.1016/j.jsb.2003.11.013
1002 Smith, M. D., Harley, M. E., Kemp, A. J., Wills, J., Lee, M., Arends, M., et al. (2018).
1003 CCPG1 Is a Non-canonical Autophagy Cargo Receptor Essential for ER-Phagy and
1004 Pancreatic ER Proteostasis. *Developmental Cell*, *44*(2), 217–232.e11.
1005 http://doi.org/10.1016/j.devcel.2017.11.024
1006 Tabb, D. L., McDonald, W. H., & Yates, J. R. (2002). DTASelect and Contrast: tools for
1007 assembling and comparing protein identifications from shotgun proteomics. *Journal*
1008 *of Proteome Research*, *1*(1), 21–26.
1009 Toyama, B. H., Arrojo e Drigo, R., Lev-Ram, V., Ramachandra, R., Deerinck, T. J.,
1010 Lechene, C., et al. (2019). Visualization of long-lived proteins reveals age
1011 mosaicism within nuclei of postmitotic cells. *The Journal of Cell Biology*, *218*(2),
1012 433–444. http://doi.org/10.1083/jcb.201809123
1013 Toyama, B. H., Savas, J. N., Park, S. K., Harris, M. S., Ingolia, N. T., Yates, J. R., III, &
1014 Hetzer, M. W. (2013). Identification of Long-Lived Proteins Reveals Exceptional
1015 Stability of Essential Cellular Structures. *Cell*, *154*(5), 971–982.
1016 http://doi.org/10.1016/j.cell.2013.07.037
1017 Tsai, P.-L., Zhao, C., Turner, E., & Schlieker, C. (2016). The Lamin B receptor is
1018 essential for cholesterol synthesis and perturbed by disease-causing mutations.
1019 *eLife*, *5*, 4181. http://doi.org/10.7554/eLife.16011

1020 Uhlen, M., Fagerberg, L., Hallstrom, B. M., Lindskog, C., Oksvold, P., Mardinoglu, A., et
1021 al. (2015). Tissue-based map of the human proteome. *Science*, *347*(6220),
1022 1260419–1260419. http://doi.org/10.1126/science.1260419
1023 Ungricht, R., Klann, M., Horvath, P., & Kutay, U. (2015). Diffusion and retention are
1024 major determinants of protein targeting to the inner nuclear membrane. *The Journal*
1025 *of Cell Biology*, *209*(5), 687–704. http://doi.org/10.1083/jcb.201409127
1026 Vaughan, A., Alvarez-Reyes, M., Bridger, J. M., Broers, J. L., Ramaekers, F. C.,
1027 Wehnert, M., et al. (2001). Both emerin and lamin C depend on lamin A for
1028 localization at the nuclear envelope. *Journal of Cell Science*, *114*(Pt 14), 2577–
1029 2590.
1030 Verzijlbergen, K. F., Menendez-Benito, V., van Welsem, T., van Deventer, S. J.,
1031 Lindstrom, D. L., Ovaa, H., et al. (2010). Recombination-induced tag exchange to
1032 track old and new proteins. *Proceedings of the National Academy of Sciences*,
1033 *107*(1), 64–68. http://doi.org/10.1073/pnas.0911164107
1034 Wang, Q., Li, L., & Ye, Y. (2008). Inhibition of p97-dependent Protein Degradation by
1035 Eeyarestatin I. *Journal of Biological Chemistry*, *283*(12), 7445–7454.
1036 http://doi.org/10.1074/jbc.M708347200
1037 Xu, T., Park, S. K., Venable, J. D., Wohlschlegel, J. A., Diedrich, J. K., Cociorva, D., et
1038 al. (2015). ProLuCID: An improved SEQUEST-like algorithm with enhanced
1039 sensitivity and specificity. *Journal of Proteomics*, *129*(C), 16–24.
1040 http://doi.org/10.1016/j.jprot.2015.07.001
1041 Zattas, D., Berk, J. M., Kreft, S. G., & Hochstrasser, M. (2016). A Conserved C-terminal
1042 Element in the Yeast Doa10 and Human MARCH6 Ubiquitin Ligases Required for
1043 Selective Substrate Degradation. *Journal of Biological Chemistry*, *291*(23), 12105–
1044 12118. http://doi.org/10.1074/jbc.M116.726877
1045 Zavodszky, E., & Hegde, R. S. (2019). Misfolded GPI-anchored proteins are escorted
1046 through the secretory pathway by ER-derived factors. *eLife*, *8*, 32.
1047 http://doi.org/10.7554/eLife.46740
1048 Zhang, K., Sha, J., & Harter, M. L. (2010). Activation of Cdc6 by MyoD is associated
1049 with the expansion of quiescent myogenic satellite cells. *The Journal of Cell Biology*,
1050 *188*(1), 39–48. http://doi.org/10.1083/jcb.200904144

1051
1052 **Supplemental Figures**
1053

Figure 1 - figure supplement 1. Half life fit examples

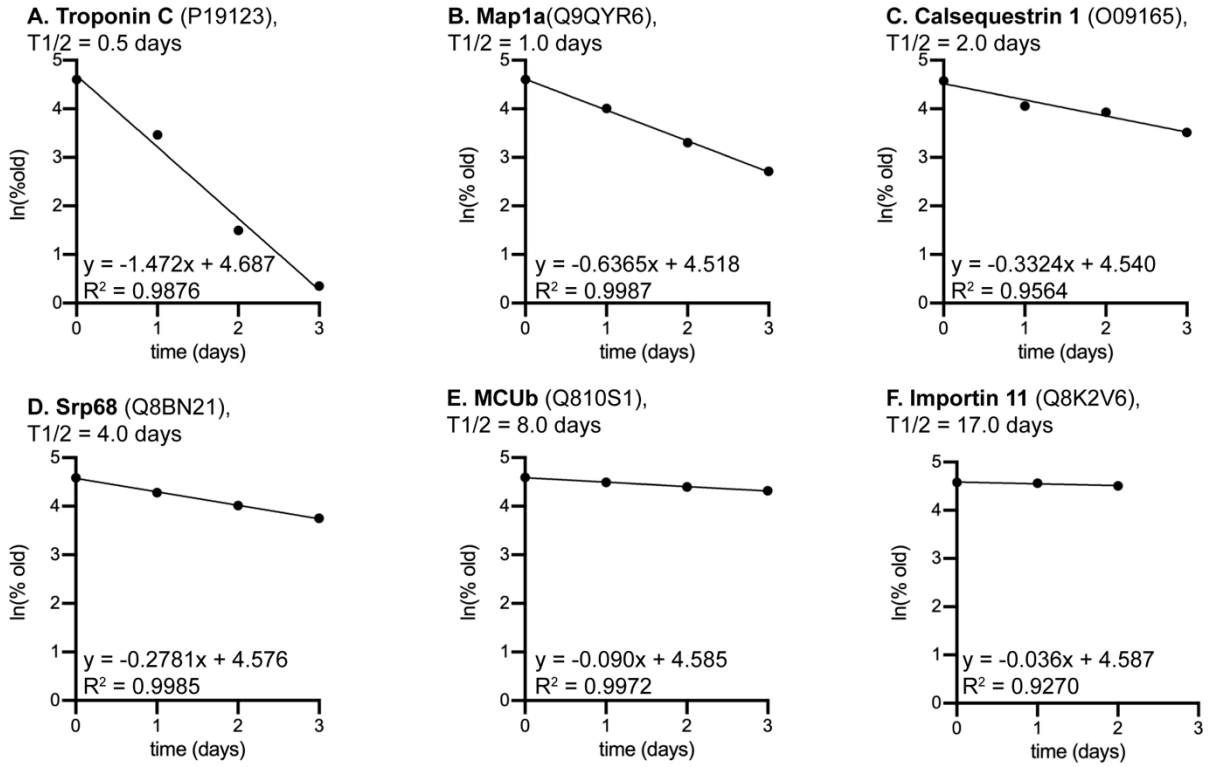

1054
1055
1056 **Figure 1 – figure supplement 1.** Example half life fits. Examples of half-life fits for
1057 proteins with predicted half-lives of 0.5 days (A), 1 day (B), 2 days (C), 4 days (D), 8
1058 days (E), and 17 days (F).
1059

Figure 2 - figure supplement 1.
Identification of a disease-linked emerin mutant with normal localization and NE residence time

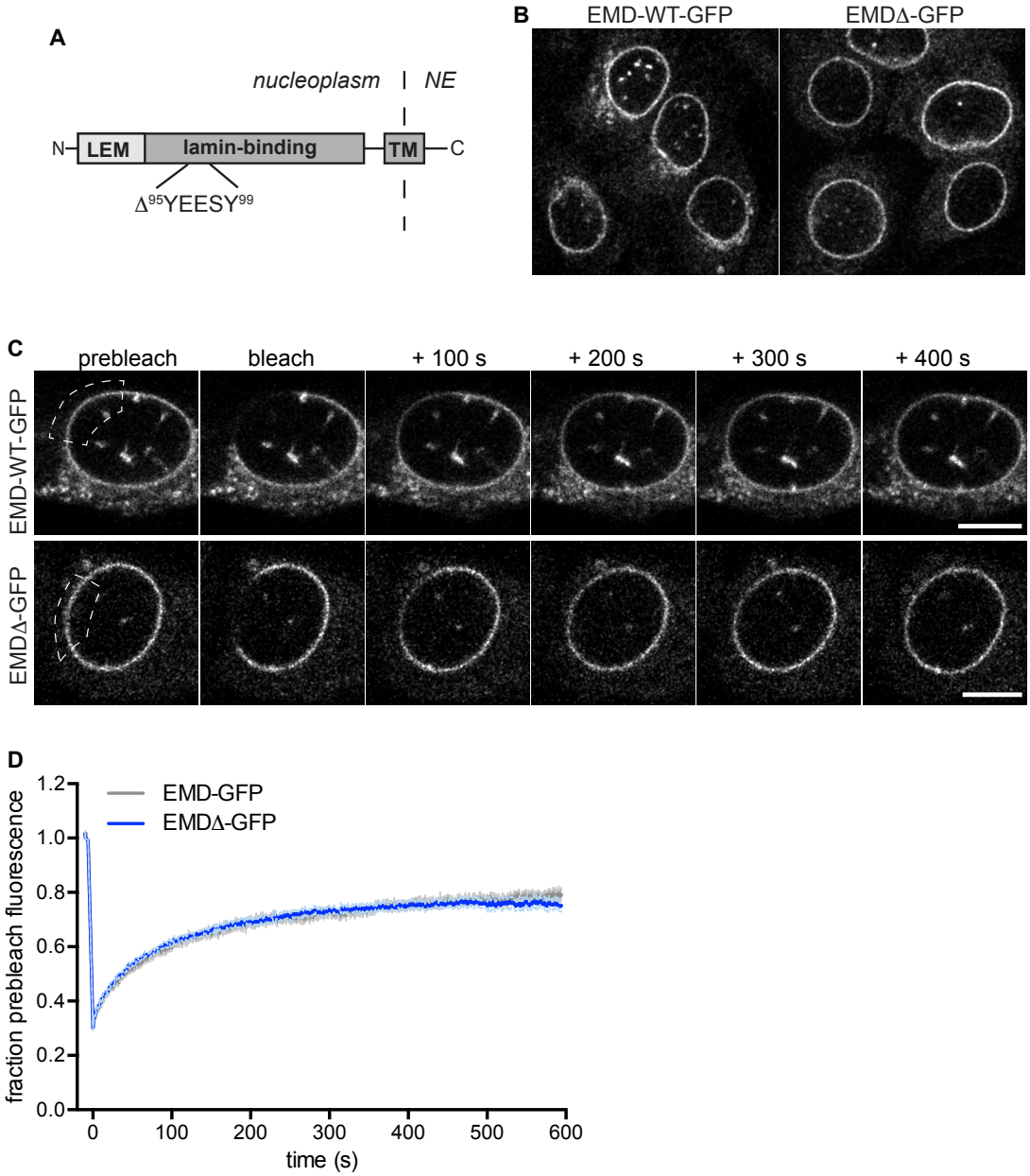

Figure 2 – figure supplement 1. Identification of a disease-linked emerin mutant with normal NE localization. (A) EMDΔ95-99-GFP (EMDΔ-GFP) has normal localization at the NE (B) and normal residence time at the NE, based on fluorescence recovery after photobleaching timecourse at the NE (C,D).

Figure 3 - figure supplement 1

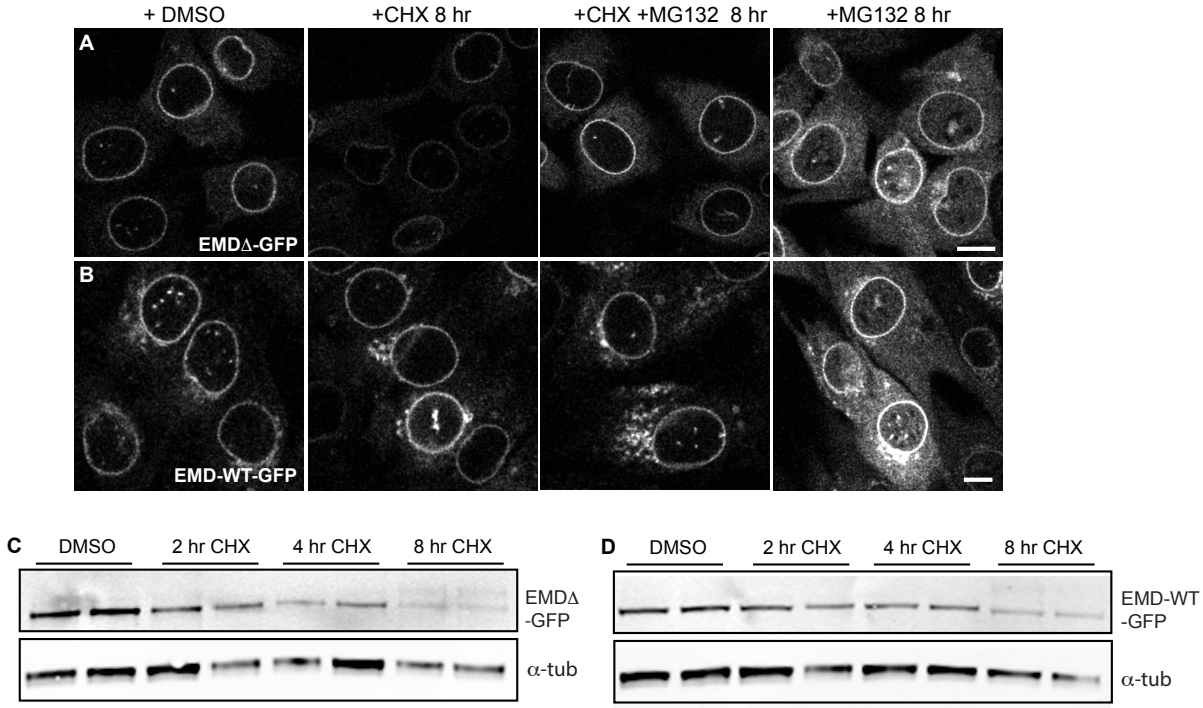

Figure 3 – figure supplement 1. Localization and stability of a disease-linked emerin variant. (A-B) C2C12 cells stably expressing EMDΔ-GFP (A) or EMD-WT-GFP (B) and treated with DMSO vehicle control, CHX alone, CHX and MG132, or MG132 alone for 8 hours. All images were acquired using the same laser power and detector gain settings. Single confocal z slices shown. Scale bar, 10 μm. (C-D) Western blot analysis of EMDΔ-GFP (C) or EMD-WT-GFP (D) protein levels after treatment with CHX for the indicates times.

Figure 3 - figure supplement 2. siRNA-mediated E2 or E3 ubiquitin ligase knockdowns do not stabilize emerin variants.

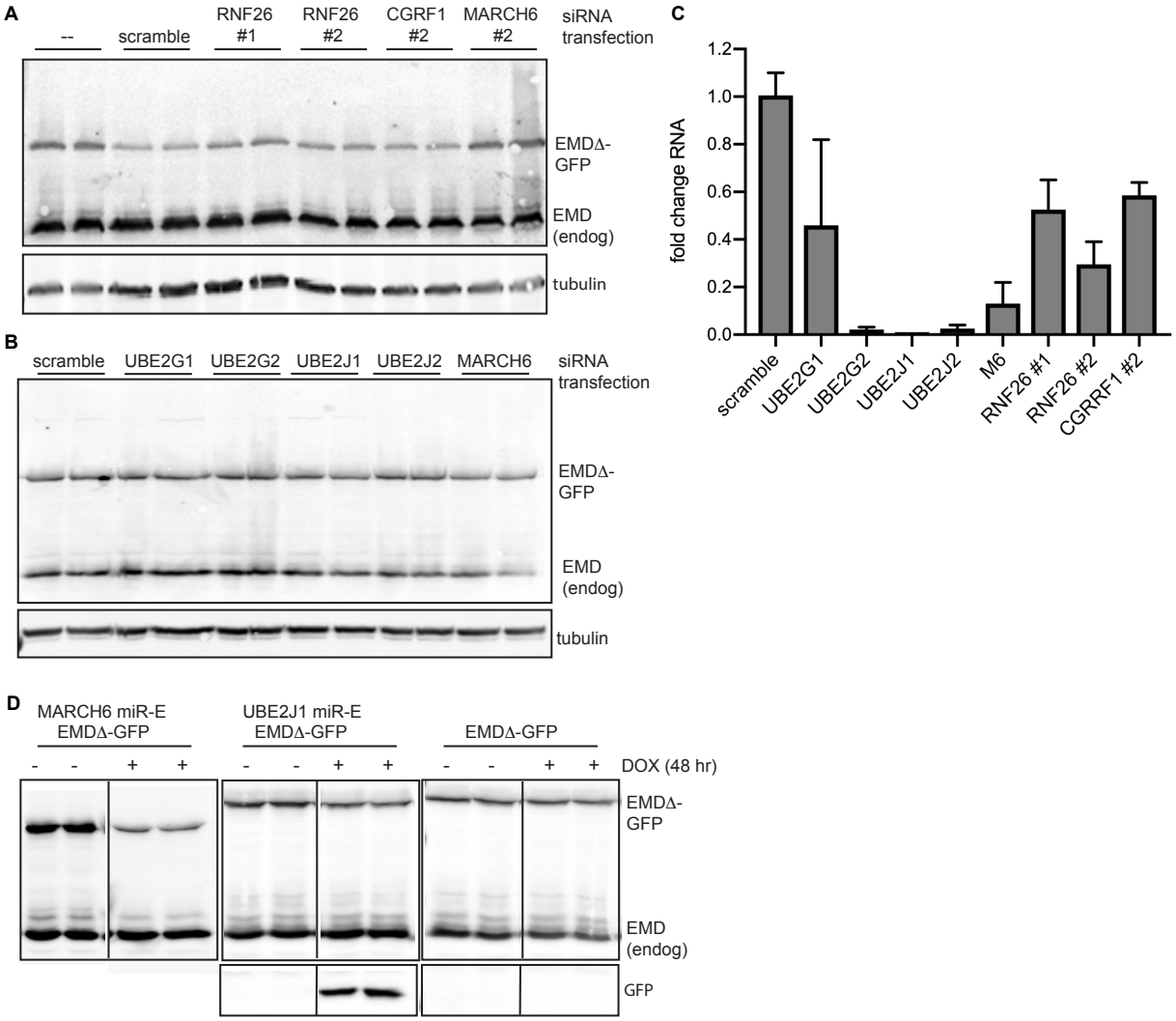

Figure 3 – figure supplement 2. siRNA-mediated E2 or E3 ubiquitin ligase knockdowns do not stabilize EMDΔ-GFP. (A-B) EMDΔ-GFP protein levels do not change in C2C12 cells stably expressing EMDΔ-GFP and transfected in duplicate with 50 nM RNAi targeting the E3 ubiquitin ligases Rnf26, CGRRF1, MARCH6, or a scrambled control (A), or targeting the E2 ubiquitin conjugating enzymes UBE2G1, UBE2G2, UBE2J1, and UBE2J2, or MARCH6 (B). (C) qPCR quantification of RNAi knockdown efficiency for conditions shown in (A-B). (D) EMDΔ-GFP protein levels either decrease or do not change in U2OS cells stably expressing EMDΔ-GFP and induced to express a miR-E RNAi cassette targeting the E3 ubiquitin ligase MARCH6 or the E2 ubiquitin conjugating enzyme UBE2J1 for 48 hours. Free GFP is also expressed from this cassette and indicates RNAi expression. miR-E RNAis used were from a validated set described in (Knott et al., Mol Cell 2014).

Figure 3 - figure supplement 3. glycosylation reporter variants are destabilized by ER stress and recovered by BFA treatment.

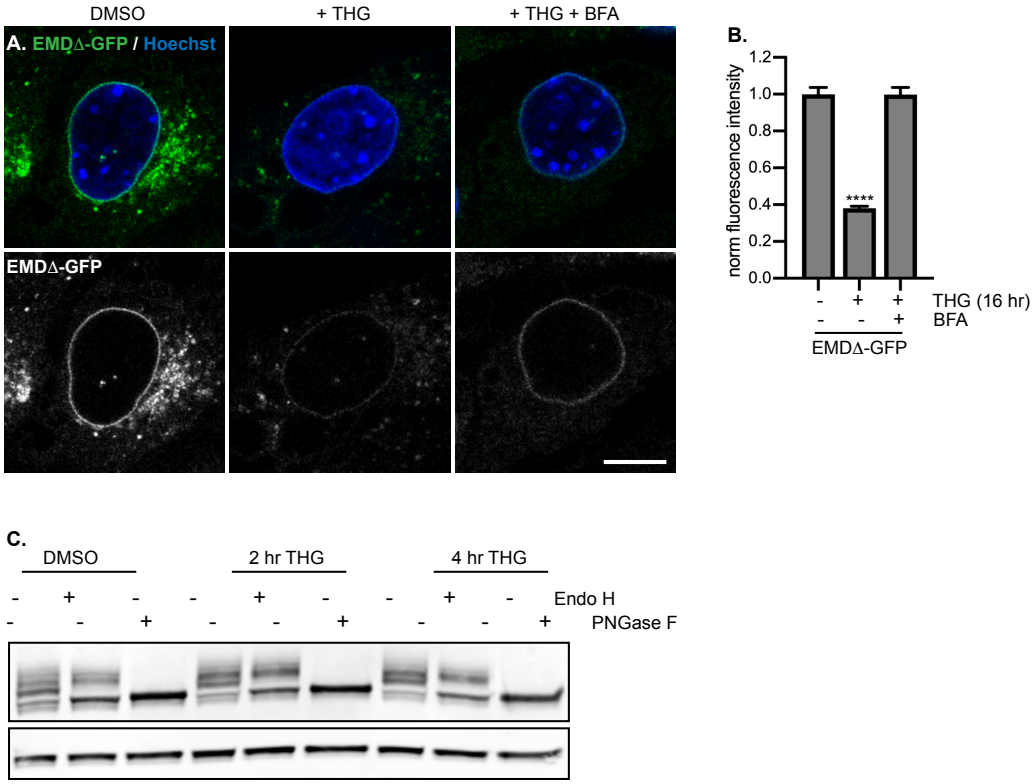

Figure 3 – figure supplement 3. Glycosylation reporter variants are destabilized by ER stress and recovered by BFA treatment. Glycosylation reporter variant of EMDΔ-GFP localizes normally to the NE and responds to ER stress induced by THG and secretory pathway disruption caused by BFA (A-B). (C) Pattern of glycosylation modifications in DMSO vehicle control treated cells or cells treated with THG for 2-4 hours. A larger proportion of EMDΔ-GFP becomes Endo H-resistant during acute ER stress.

Figure 4 - figure supplement 1

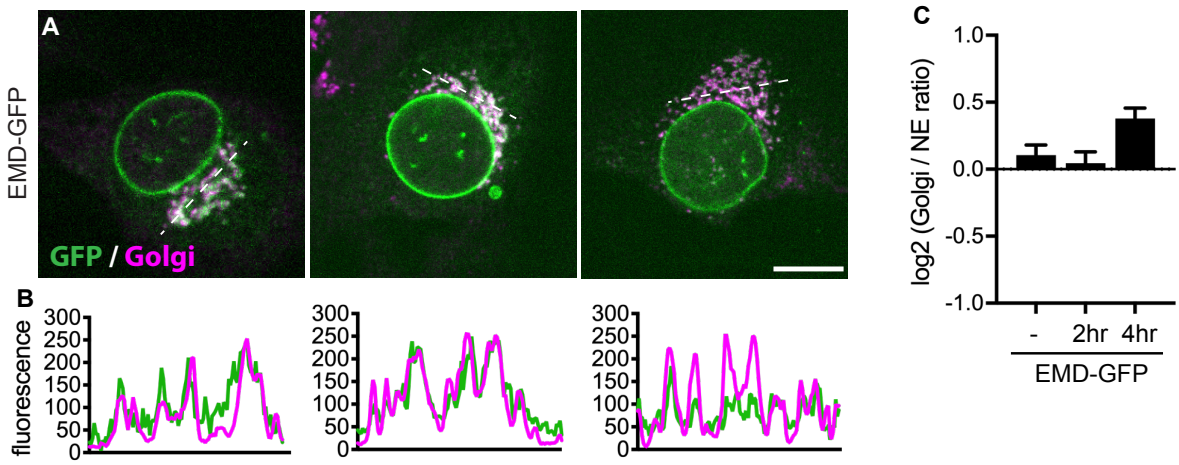

Figure 4 – figure supplement 1. Colocalization of emerin with the Golgi. (A-B) Representative confocal slices of cells stably expressing EMD-WT-GFP, treated with DMSO or THG for the indicated times and costained for giantin to mark the Golgi (magenta). All images were acquired using the same laser power and detector gain settings. Dotted lines mark positions of linescans shown in (B). (C) Quantification of GFP fluorescence intensity abundance ratio in Golgi versus NE in single, non-contrast-adjusted z slices over THG treatment timecourse. Columns indicate average with error bars indicating SEM for N > 47 cells from 2 independent experiments. **** indicates p-value < 0.0001. Scale bars in micrographs indicate 10 μm.

Figure 6 - figure supplement 1

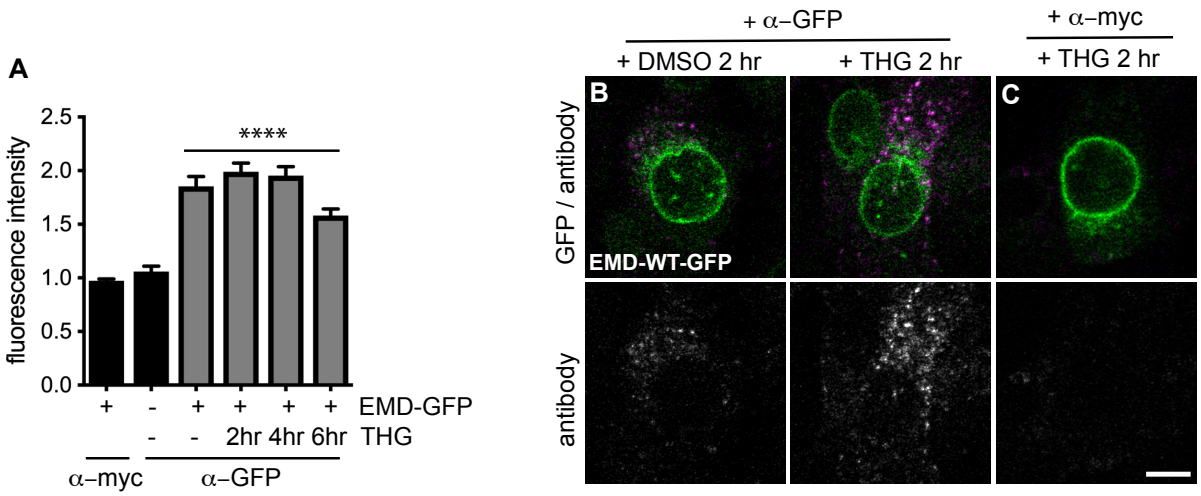

Figure 6 – figure supplement 1. Access of emerin to the plasma membrane. (A) Uptake of anti-GFP antibody (magenta) by cells stably expressing EMD-WT-GFP and treated with DMSO vehicle control or THG for the indicated times. Cells were incubated with anti-GFP antibody for the final hour of the treatment period before fixation and imaging. (B) control demonstrating lack of uptake of anti-myc antibody by cells stably expressing EMD-WT-GFP and treated with THG for 2 hours. (D) Quantification of internalized antibody signal in EMD-WT-GFP expressing cells. Columns indicate average and error bars indicate SEM for N > 66 cells from 2 independent experiments. **** indicates 2-value < 0.0001 (t-test) compared to untreated.

Figure 7 - figure supplement 1. glycosylation reporter variants are destabilized by ER stress and recovered by BFA treatment.

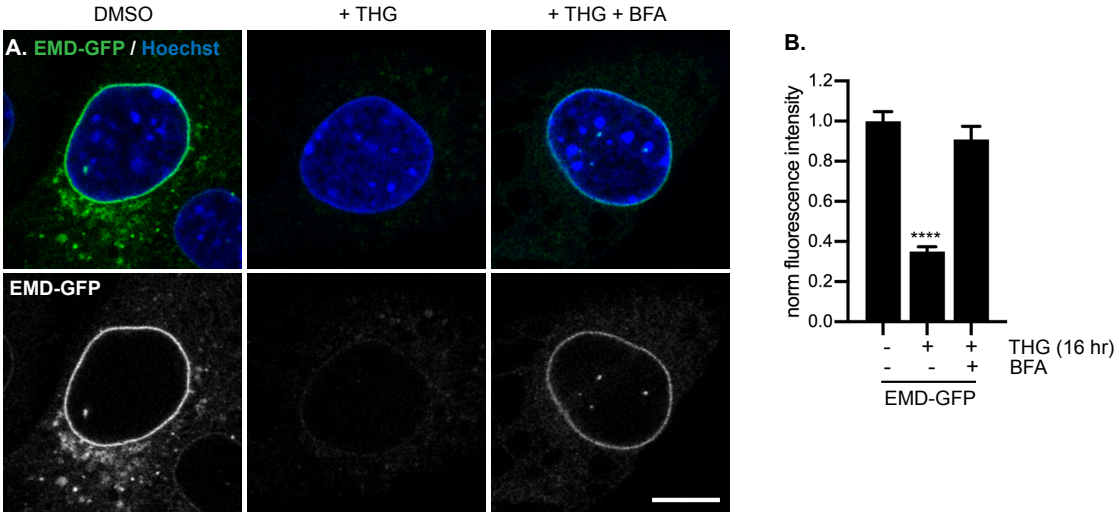

Figure 7 – figure supplement 1. Glycosylation reporter variants are destabilized by ER stress and recovered by BFA treatment. (A-B) Glycosylation reporter variant of EMD-WT-GFP localizes normally to the NE and responds to ER stress induced by THG and secretory pathway disruption caused by BFA.

Figure 8 - figure supplement 1

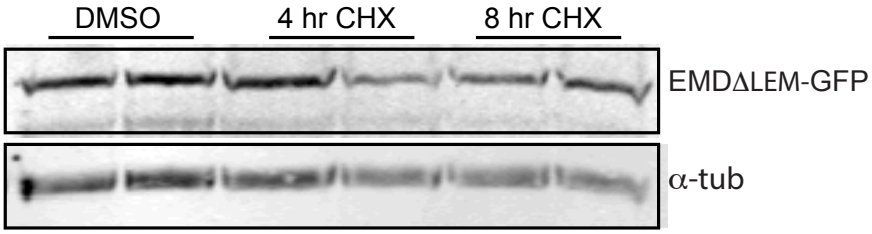

Figure 8 – figure supplement 1. Stability of EMDΔLEM-GFP over time of cycloheximide treatment. Western blot detection of EMDΔLEM-GFP protein levels in cells treated with DMSO vehicle control or CHX for the indicated times.

Figure 8 - figure supplement 2. emerin is mislocalized to the ER but not degraded in lmna -/- MEFs.

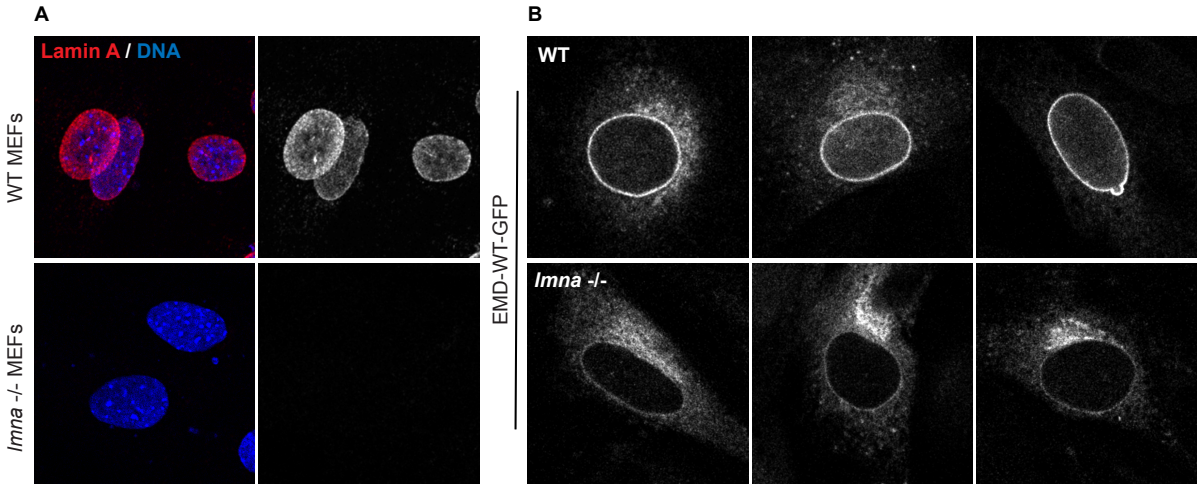

1141
1142 **Figure 8 – figure supplement 2.** Emerin is mislocalized to the ER, but not degraded in
1143 *lmna -/-* MEFs. (A) representative immunostaining of WT MEFs or of *lmna -/-* MEFs with
1144 lamin A antibody (red) and Hoechst (blue). (B) Representative immunofluorescence of
1145 EMD-GFP stably expressed in WT MEFs (top panel) or *lmna -/-* MEFs (bottom panel).
1146
1147 **Source Data 1.** Filtered peptide data for half life calculations. Peptide turnover data for
1148 all peptides passing quality control filters. See R script and Methods for details.
1149
1150 **Source Data 2.** Filtered protein data for half life calculations. Filtered and averaged
1151 protein turnover data. See R script and Methods for details.
1152
1153 **Supplementary File 1.** Results of half life fits passing quality filters.
1154
1155 **Supplementary File 2.** Complete list of half life fits.
1156
1157 **Supplementary File 3.** Half lives and protein topology data. Selected data related to
1158 Figure 1G-H.